

# Geochemistry, Geophysics, Geosystems®



## RESEARCH ARTICLE

10.1029/2022GC010732

### Key Points:

- Sr-isotopes in plagioclase record the emergence of eruptible magma through amalgamation of pre-existing mush in the Central Andes
- The amalgamated magma did not reside at depth for longer than centuries to millennia based on diffusion chronometry
- Forward modeling indicates that high-precision gravity monitoring has large potential to resolve eruptible magma amalgamation

### Supporting Information:

Supporting Information may be found in the online version of this article.

### Correspondence to:

G. Weber,  
[gregor\\_weber@gmx.de](mailto:gregor_weber@gmx.de)

### Citation:

Weber, G., Blundy, J., & Bevan, D. (2023). Mush amalgamation, short residence, and sparse detectability of eruptible magma before Andean super-eruptions. *Geochemistry, Geophysics, Geosystems*, 24, e2022GC010732. <https://doi.org/10.1029/2022GC010732>

Received 5 OCT 2022

Accepted 1 JAN 2023

### Author Contributions:

**Conceptualization:** G. Weber, J. Blundy

**Data curation:** G. Weber

**Formal analysis:** G. Weber

**Funding acquisition:** G. Weber, J. Blundy

**Investigation:** G. Weber, J. Blundy, D. Bevan

**Methodology:** G. Weber

**Project Administration:** G. Weber

**Software:** G. Weber

**Visualization:** G. Weber

**Writing – original draft:** G. Weber

© 2023 The Authors.

This is an open access article under the terms of the [Creative Commons Attribution-NonCommercial License](https://creativecommons.org/licenses/by-nc/4.0/), which permits use, distribution and reproduction in any medium, provided the original work is properly cited and is not used for commercial purposes.

## Mush Amalgamation, Short Residence, and Sparse Detectability of Eruptible Magma Before Andean Super-Eruptions

G. Weber<sup>1</sup> , J. Blundy<sup>1</sup> , and D. Bevan<sup>2</sup>

<sup>1</sup>Department of Earth Sciences, University of Oxford, Oxford, UK, <sup>2</sup>School of Earth Sciences, University of Bristol, Bristol, UK

**Abstract** Giant volcanic eruptions have the potential to overturn civilizations. Yet, the driving mechanism and timescale over which batholithic magma reservoirs transition from non-eruptible crystal mush to mobile melt-dominated stages and our capacity to detect a pending super-eruption remain obscure. Here we show, using Sr isotope zonation in plagioclase crystals from three Andean large-magnitude eruptions (Atana, Toconao, and Tara ignimbrites), that eruptible magma forms by amalgamation of isotopically diverse crystal populations and silicic melt without large-scale reheating. In each case, crystals record large isotopic diversity in crystal cores, converging toward a common value in crystal rims that coincides with the composition of the rhyolitic carrier melt. Using diffusion chronometry, we show that the assembled magma resided pre-eruptively in the crust for timescales of no more than decades to centuries for Atana and Tara, but up to several millennia for Toconao. These timescales and isotopic observations are consistent with the accumulation and destabilization of melt-rich layers in crystal mush. While the prospect of capturing such melt lenses with most geophysical monitoring techniques is pessimistic, gravity modeling indicates that such structures are potentially resolvable. Our findings provoke a new assessment of the origin and hazards associated with large magnitude explosive eruptions.

**Plain Language Summary** Super-eruptions are the largest manifestation of explosive volcanism on Earth. If such an event would occur today, it could deeply impact human civilization on a global scale. Yet, signals that may emerge prior to such eruptions are difficult to constrain. To gain greater understanding of the mechanisms and timescales over which giant, eruptible, reservoirs form, and to evaluate our capacity of capturing the evolution toward large eruptions, we studied plagioclase crystals, a mineral that is an excellent recorder of magmatic processes. For three large eruptions in the Central Andes, we analyzed strontium isotopes in traverses from crystal cores to rims to provide a temporal record of melt composition. Our results show that, in each case, the eruptible magma amalgamated from distinct pre-existing magma pockets that merged prior to eruption. This merged state of the magma did not exist for longer than a few hundred to thousands of years based on the preservation of the crystal strontium-isotope traverses at high temperatures. These results are consistent with the destabilization of melt-rich layers on timescales comparable to human lifespans. Although most geophysical imaging methods are unlikely to capture this process, our calculations indicate that gravity monitoring of super-volcanoes can potentially resolve such structures.

## 1. Introduction

Earth history is punctuated by voluminous outbursts of magma, commonly termed super-eruptions, when a dense rock equivalent volume of more than 450 km<sup>3</sup> is discharged explosively at the surface (Self, 2006; Sparks et al., 2022; Wilson et al., 2021). Such events are rare but will inevitably occur again in the future with severe consequences for life on Earth (Black et al., 2021; Papale, 2018; Rampino, 2002; Self & Blake, 2008). While several volcanoes capable of producing such eruptions have been identified, the processes and timescales over which such systems transition from dormancy to eruption are not well understood. Better constraints on magmatic processes and timescales are crucial to evaluate our capacity to capture the evolution toward large magnitude eruptions using geophysical monitoring techniques and resolve potential eruption harbingers.

A prerequisite to producing a supereruption is that sufficiently large volumes of eruptible magma (i.e., magma with typically <50% crystallinity) accumulate in the Earth's crust (Annen, 2009; Bachmann & Bergantz, 2008; Barker et al., 2016; Caricchi et al., 2014; Dufek & Bachmann, 2010; Marsh, 1981; Vigneresse et al., 1996).

Writing – review & editing: J. Blundy,  
D. Bevan

However, the search for such high melt fraction anomalies by geophysical methods has to date been inconclusive (Magee et al., 2018), providing one of the various lines of evidence to the widely recognized notion that magmatic systems spend most of their lifespan in a crystal-rich non-eruptible state (i.e., crystal mush) (Bachmann & Bergantz, 2004, 2008; Bachmann & Huber, 2019; Cashman et al., 2017; Edmonds et al., 2019; Jackson et al., 2018). Such crystal mushes are comprised of a rigid crystal framework and interstitial melt, which due to rheological impediments are not eruptible until some melt mobilization process takes place, the nature of which is still widely debated (Barker et al., 2016; Burgisser & Bergantz, 2011; Gualda & Sutton, 2016; Pistone et al., 2017; Rubin et al., 2017; Sisson & Bacon, 1999; Spera & Bohrson, 2018; Szymanowski et al., 2017; Wotzlaw et al., 2014).

Geochemical observations and theoretical modeling have been used to argue for both long (several hundred ka) and short (month to centuries) timescales for the transition from mush to eruptible magma. Intrusion of hot mafic magma into or beneath crystal mushes may induce melting and reduce the fraction of crystals present in such systems, thereby increasing eruptibility. Support for this hypothesis, commonly termed “thermal rejuvenation,” has been derived from the resorption or absence of mineral phases in the erupted rock (Bachmann et al., 2002; Sliwinski et al., 2019) or in the form of time-temperature reconstructions based on zircon dating and trace element chemistry (Claiborne et al., 2010; Klemetti & Clynne, 2014; Szymanowski et al., 2017, 2019; Tapster et al., 2016; Wotzlaw et al., 2013, 2014). Thermodynamic and fluid mechanical models of thermal reactivation processes require timescales of 1,000–10,000s of years (Huber et al., 2011; Spera & Bohrson, 2018), consistent with zircon-derived estimates, showing evidence for an evolution toward higher temperatures prior to large eruptions. However, temperature increases over such timescales may also reflect the long-term thermal maturation of magma reservoirs during their assembly, which for moderate magma fluxes will inevitably lead to increasing temperatures with time without the need of a causative rise in crustal magma injection rates (Annen et al., 2006; P.-P. Liu et al., 2021; Lukács et al., 2021; Weber, Caricchi, et al., 2020; Weber, Simpson, & Caricchi, 2020). Crystal-scale studies that employ modeling of the diffusive relaxation of elemental concentrations in various mineral phases, frequently find evidence for the assembly of eruptible magma on timescales of decades to centuries prior to volcanic eruptions, independent of their size (Allan et al., 2013, 2017; Chamberlain et al., 2014; Cooper et al., 2017; Druitt et al., 2012; Rubin et al., 2017; Shamloo & Till, 2019). While it has been argued that such short timescales are inconsistent with thermal rejuvenation and may reflect single magma recharge events rather than the assembly of eruptible magma (Spera & Bohrson, 2018), numerical models of the growth and destabilization of melt-rich layers in crystal mush do not require large-scale reheating and are consistent with rapid timescales (Burgisser & Bergantz, 2011; Jackson et al., 2018; Seropian et al., 2018).

Mineral-scale reconstructions of the processes and pace of eruptible magma assembly prior to volcanic eruptions can be ambiguous due to multiple, aliased dependencies (e.g., pressure, temperature, melt chemistry,  $fO_2$ ,  $\alpha H_2O$ ) that may blur the interpretation of such records. We take advantage of recent technical improvements in the capability to measure in situ Sr isotope ratios in plagioclase crystals (Bevan et al., 2021), a record that is only dependent on melt isotopic composition during crystal growth and is consequently less ambiguous to interpret than simple elemental crystal zonation patterns (e.g., Chadwick et al., 2007; Charlier et al., 2007; Davidson et al., 2001, 2007; Ramos et al., 2005; Tepley et al., 2000; Waight & Tørnqvist, 2018). We show here that the crystal cargo of three ignimbrite-forming eruptions from the Altiplano-Puna Volcanic Complex (Central Andes), originated from spatially and/or temporally separated magma batches that were merged by mingling with a common rhyolitic melt prior to eruption without evidence for thermal rejuvenation. Using diffusion chronometry, we estimate that the final assembled magma resided pre-eruptively in the Earth's crust for no more than a few decades to millennia. Finally, we discuss and evaluate our capacity to capture the evolution toward large magnitude eruptions using state-of-the-art geophysical methods.

## 2. Regional Context: Altiplano-Puna Magma Body and Ignimbrites

Recent geophysical and geodetic surveys have revealed a colossal, active magma reservoir beneath the Altiplano-Puna highland of Northern Chile and Bolivia (Figure 1), known as the Altiplano Puna Magma Body (APMB) and comprising a volume of roughly 500,000 km<sup>3</sup> of partially molten rock with melt fraction of about 20 vol% (Pritchard et al., 2018). Over the last 10 million years the overlying area, referred to as Altiplano-Puna Volcanic Complex (APVC), has been one of the most productive volcanic regions on Earth with extensive deposits of voluminous pyroclastic density currents (or ignimbrites) (Brandmeier & Wörner, 2016; de Silva & Kay, 2018; De Silva et al., 2006; Kay et al., 2010; Kern et al., 2016; Salisbury et al., 2011). A direct relationship of the APVC

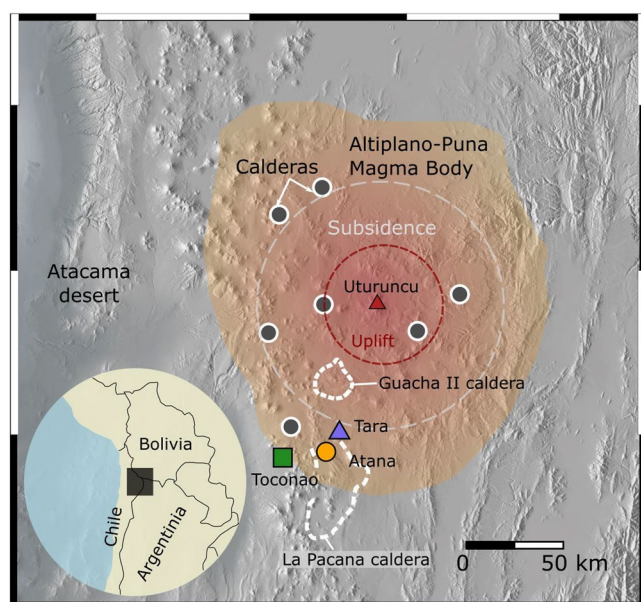


**Figure 1.** Sampling locations of the Atana (orange circle), Tara (purple triangle), and Toconao (green square) ignimbrites in the Altiplano-Puna Volcanic Complex. Outlines of the La Pacana and Guacha II calderas are indicated by white dashed lines, while other calderas in the area are marked as gray dots. The extent of the mid-crustal Altiplano-Puna Magma body at 15 km depth (Ward et al., 2014) is projected onto the relief map. Ground deformation pattern, centered at Uturuncu volcano in Bolivia (red triangle), are shown as red (uplift) and gray (subsidence) dashed lines (Pritchard et al., 2018). The inset shows the location of the study area in the border region between Chile, Argentina, and Bolivia. Relief Map was modified from MFF-maps under Creative Commons CC0.

to the APMB can be inferred from the juxtaposition of large silicic caldera complexes and the inferred geophysical anomaly (Figure 1), as imaged by seismic, gravity and magnetotelluric techniques (Comeau et al., 2015, 2016; del Potro et al., 2013; Ward et al., 2014, 2017; Zandt et al., 2003). Large scale ground deformation centered at Uturuncu stratovolcano in the central APVC, has been observed over the last 20 years, testifying to the active nature of the APMB (Gottsmann et al., 2017; Hickey et al., 2013; Perkins et al., 2016). In this study, we focus on three large eruptions in the APVC that span a range of bulk-rock compositions and volumes: the dacitic Atana and Tara, and rhyolitic Toconao ignimbrites.

The Atana and Toconao ignimbrites have been traced back to a source within the 60 to 35 km wide La Pacana caldera complex in Northern Chile (Gardeweg & Ramírez, 1987; Lindsay, de Silva, et al., 2001; Lindsay, Schmitt, et al., 2001). With an estimated dense rock equivalent (DRE) volume of 1,600 km<sup>3</sup>, the Atana ignimbrite is the most voluminous eruption known in the Central Andes (Brandmeier & Wörner, 2016; Lindsay, de Silva, et al., 2001; Lindsay, Schmitt, et al., 2001), marking the peak conditions in the flare-up of large magnitude eruptions that this region has experienced over the last 10 Ma (de Silva & Kay, 2018; de Silva & Gosnold, 2007). Volume estimates for the Toconao eruption have been challenging due to limited exposure, but the preserved outflow sheet has a volume of about 180 km<sup>3</sup> (Lindsay, de Silva, et al., 2001; Lindsay, Schmitt, et al., 2001). <sup>40</sup>Ar/<sup>39</sup>Ar dating of biotite grains has constrained the isochron age of the Atana eruption to 3.92 ± 0.14 Ma (Salisbury et al., 2011). Although high precision geochronology is currently not available for the Toconao eruption, its stratigraphic position below the Atana ignimbrite, K-Ar dating and U-Pb ages of zircon crystals indicate eruption between 4.0 and 4.5 Ma (de Silva, 1989; Kern et al., 2016). Thus, the Toconao and Atana ignimbrites could have been erupted in rapid succession. Mineral thermobarometry has been used to constrain a pre-eruptive pressure of 200 MPa and temperatures for the Atana and Toconao ignimbrites to be 770–790°C and 730–750°C, respectively (Lindsay, Schmitt, et al., 2001). Like other Central Andean ignimbrites, initial (i.e., time-corrected) whole-rock <sup>87</sup>Sr/<sup>86</sup>Sr compositions are highly heterogeneous for different whole-rock samples but overlapping for the Atana and Toconao eruptions within the range 0.7093–0.7131, confirming an important petrogenetic role of crustal assimilation, in keeping with other silicic magmas of the APVC (Brandmeier & Wörner, 2016; Freymuth et al., 2015; Kay et al., 2010; Lindsay, Schmitt, et al., 2001; Schmitt et al., 2001).

The dacitic Tara ignimbrite is sourced from the 20 × 30 km wide Guacha II Caldera in Bolivia and is part of the larger nested Cerro Guacha caldera complex (Grocke, de Silva, Iriarte, et al., 2017; Grocke, de Silva, Wallace, et al., 2017) that lies approximately 35 km north of La Pacana. A minimum DRE volume of 800 km<sup>3</sup> has been constrained for the Tara eruption (Grocke, de Silva, Iriarte, et al., 2017; Grocke, de Silva, Wallace, et al., 2017), placing it halfway between the Atana and Toconao eruptions and other ignimbrites in the APVC. Radiometric dating by the <sup>40</sup>Ar/<sup>39</sup>Ar technique indicates eruption at 3.49 ± 0.01 Ma (Salisbury et al., 2011), consistent with the youngest U-Pb zircon age (Kern et al., 2016). Quartz-hosted melt inclusion analysis has been used to constrain pre-eruptive water contents of up to 6.0 wt.% H<sub>2</sub>O, consistent with magma storage pressures of about 200 MPa and temperatures of 800–850°C, as derived from amphibole thermobarometry (Grocke, de Silva, Iriarte, et al., 2017; Grocke, de Silva, Wallace, et al., 2017). <sup>87</sup>Sr/<sup>86</sup>Sr-isotope ratios of bulk-rock samples span the range 0.709380–0.713159, similar to the observed variability for the Atana and Toconao eruptions.

### 3. Materials and Methods

#### 3.1. Sample Collection and Processing

Samples of the Atana, Toconao, and Tara ignimbrites studied in this contribution were collected during a field campaign in Northern Chile in 2018. Photographic documentation of sampling locations can be found in Figure

S1 of Supporting Information S1. The Atana ignimbrite sample was collected on the western flank of Cerro La Pacana, the resurgent dome of the caldera, at  $4,739 \pm 4$  m altitude along a roadcut on Ruta 27 (GPS coordinates:  $23^{\circ}06'27.83''\text{S}$ ,  $067^{\circ}29'42.13''\text{W}$ ). The Tara ignimbrite was sampled inside the moat of the La Pacana caldera, where it occurs as isolated pillars and steep erosional cliffs (altitude:  $4,541 \pm 4$  m; GPS coordinates:  $23^{\circ}03'19.13''\text{S}$ ,  $067^{\circ}29'46.63''\text{W}$ ). Sampling of the Toconao ignimbrite was carried out in its type locality at Quebrada de Jerez, 1 km east of Toconao village (altitude:  $2,531 \pm 4$  m; GPS coordinates:  $23^{\circ}11'18.86''\text{S}$ ,  $067^{\circ}59'31.11''\text{W}$ ). The samples were processed to separate pumice-hosted plagioclases by crushing the rocks using a sledgehammer and hydraulic press at the University of Geneva, Switzerland. The crushed samples were washed in de-ionized water and dried in an oven at  $40^{\circ}\text{C}$ , before sieving to a size fraction  $>1$  mm. Plagioclase crystals were then handpicked under a binocular microscope, mounted in epoxy resin, and polished in several steps under water and with diamond paste. Additionally, ignimbrite pumices were separated, mounted, and polished using the same methodology as for the plagioclase grains.

### 3.2. Electron-Beam Techniques

The epoxy mounts were coated with a 20 nm thick layer of carbon prior to imaging and analysis with electron beam techniques. Back-scattered electron (BSE) images of plagioclase zonation textures were acquired using a JEOL JXA 8200 Electron Probe Microanalyzer (EPMA) at 15 kV acceleration voltage and 15–20 nA beam current at the University of Geneva and using a JEOL JXA 8200 EPMA at the Research Laboratory for Archeology and History of Art, University of Oxford. Quantitative EPMA traverses were obtained using a Cameca SX100 instrument at the University of Bristol (UK) and a JEOL JXA 8200 at the Research Laboratory for Archeology and History of Art (University of Oxford, UK) by wavelength-dispersive x-ray spectrometry (WDS). Primary calibration was carried out on Albite (Na, Si, Al), Sanidine (K), MgO (Mg), and Andradite (Fe, Ca). All measurements were obtained with an electron beam focused to  $\sim 2$   $\mu\text{m}$ , beam current of 15–20 nA and acceleration voltage of 15 kV. Peak counting times were 20 s for Na, 30 s for Si, Al, K, Ca, Fe (Oxford), and 10 s for Na, Si, K, Ca, 20 s for Al, and 60 s for Fe (Bristol). Background count times were one half of peak in all cases. The instruments were calibrated by repeated measurements of in-house standards, which were also analyzed at the beginning, during and at the end of the plagioclase analyses (Table S1b in Data Set S1). The external reproducibility based on repeated analysis of plagioclase and glass secondary standards was  $<1\%$  relative for  $\text{SiO}_2$ ,  $<4\%$  for  $\text{Na}_2\text{O}$ ,  $<6\%$  for  $\text{K}_2\text{O}$ ,  $<5\%$  for  $\text{FeO}$ , and  $<1\%$  for  $\text{Al}_2\text{O}_3$  and  $\text{CaO}$ . Measurements that showed totals outside the range 98.5–101.5 wt.% were discarded.

### 3.3. In Situ Sr Isotope Analysis

The in situ Sr isotope analysis of plagioclase grains and groundmass glasses was conducted at the Bristol Isotope Group mass spectrometry laboratory in the University of Bristol. The Sr isotope analysis was carried out using Proteus, a unique collision cell, multicollector inductively coupled plasma mass spectrometer with a pre collision cell, quadrupole mass filter (CC-MC-ICPMS/MS), coupled to a Teledyne<sup>TM</sup> Photon Machines 193 nm Analyte G2<sup>TM</sup> ArF excimer laser ablation system equipped with an aerosol rapid introduction system (ARIS) (Bevan et al., 2021).

The standard laser ablation conditions used for sampling were a laser fluence of  $6 \text{ J cm}^{-2}$ , a repetition rate of 10 Hz, and laser pulse count of 600. The laser spot diameter varied between 50 and 85  $\mu\text{m}$ . Carrier gas used for the laser analysis was He at a flow rate of 0.9 L/min. To quantify the compositional variation across different mineral zones and to match the EPMA traverses, laser ablation spot transects were positioned from plagioclase core to rim, perpendicular to zoning interfaces visible using back scatter electron (BSE) imaging. Each analysis was conducted using a fixed laser spot position. To exclude any periods of washout a single measurement cycle at the beginning and the end of ablation was rejected from the data.

During analysis the Proteus pre collision cell quadrupole was operated in band-pass mode, only permitting the stable ion transmission of  $87 \pm 5$  u/e (unified atomic mass units per electronic charge) onward into the collision cell. Sulfur hexafluoride ( $\text{SF}_6$ ) was utilized as the collision cell reaction gas to provide chemical resolution of Rb and Sr ions during analysis. This gas was demonstrated to display no observable reaction with  $\text{Rb}^+$  and exhibits an efficient exothermic reaction with  $\text{Sr}^+$  to form  $\text{SrF}^+$  (Bevan et al., 2021). The reaction gas mixture used was 5%  $\text{SF}_6$  (99.99% purity) in He (99.9999% purity) which was further diluted using a separate He gas cylinder



(99.999% purity). Total He and SF<sub>6</sub> collision cell gas flows used during analysis were 3 and 0.03 ml min<sup>-1</sup>. The use of SF<sub>6</sub> as a reaction gas to provide Rb and Sr chemical resolution is so efficient that no <sup>87</sup>RbF correction is required in samples with ≤Rb/Sr = 100 (Bevan et al., 2021). Thus, no <sup>87</sup>RbF correction was applied to the data presented here.

A “low-resolution” aperture slit (DM/M~3000, 5%–95% peak height definition) was used for all analysis, as this provides sufficient mass resolving power to avoid any measurement of collision cell-derived SF<sub>3</sub>O<sup>+</sup> isobaric interferences. To enhance Sr ion sensitivity a cold plasma Ni skimmer cone was used (Bevan et al., 2021). Ion beam collection was achieved using an array of Faraday cup collectors, equipped with 10<sup>11</sup> Ω feedback resistors, in a static measurement configuration. A total measurement integration time of ~60 s was used for all analyses. Measured <sup>87</sup>SrF<sup>+</sup>/<sup>86</sup>SrF<sup>+</sup> ratios were internally normalized to an <sup>86</sup>Sr/<sup>88</sup>Sr ratio of 0.1194 using the exponential mass fractionation law (Russell et al., 1978) and the atomic Sr masses. The internally normalized <sup>87</sup>Sr/<sup>86</sup>Sr ratios for the sample plagioclase and glass were externally normalized to internally normalized measurements of in-house plagioclase standard Te-1 and glass standard BHVO-2G respectively. Reference <sup>87</sup>Sr/<sup>86</sup>Sr values determined by previous thermal ionization mass-spectrometry of 0.704000 for Te-1 (Bevan et al., 2021) and 0.703469 (Elburg et al., 2005) for BHVO-2G were used when externally normalizing sample <sup>87</sup>Sr/<sup>86</sup>Sr ratios. This external normalization was carried out to correct for any residual instrumental artifacts after internal normalization (Bevan et al., 2021). Secondary standard analysis of BCR-2G, BHVO-2G and Te-1 are provided in electronic supplementary Table S2b in Data Set S1. The secondary <sup>87</sup>Sr/<sup>86</sup>Sr ratios remain within uncertainty (2SD) of the thermal ionization mass spectrometry reference values during 31 of the 33 samples analyzed. The inaccuracy of measured <sup>87</sup>Sr/<sup>86</sup>Sr ratios for BCR-2G during analysis of Atana plagioclase 2 and 3 transect 1 was a result of residual oxygen contamination in the SF<sub>6</sub> collision cell gas line. The presence of oxygen in the collision cell of Proteus promotes the formation of <sup>89</sup>Y<sup>16</sup>O<sup>+</sup> ions which act as an isobaric interference for collected <sup>86</sup>Sr<sup>19</sup>F<sup>+</sup>, which is used in calculation of <sup>87</sup>Sr/<sup>86</sup>Sr ratios (described as an issue previously in Bevan et al. (2021)). This interference resulted in our calculated BCR-2G <sup>87</sup>Sr/<sup>86</sup>Sr ratios being biased too unradiogenic relative to the reference value for this standard (Elburg et al., 2005). After lengthy purging of collision cell gas lines (the same procedure described in Bevan et al. (2021)) the <sup>87</sup>Sr/<sup>86</sup>Sr ratio for the secondary standards then remains accurate during the analysis of the remaining 31 samples. The results for Atana plagioclase 2 and 3 transect 1 are included due to the significantly lower Y/Sr expected for plagioclase relative to the BCR-2G basaltic glass, due to the very high partition coefficient ratio D<sub>Sr</sub>/D<sub>Y</sub> into plagioclase (Dohmen & Blundy, 2014). Therefore, despite the inaccuracy in BCR-2G secondary standard data we expect the impact of any <sup>89</sup>Y<sup>16</sup>O<sup>+</sup> interference to be negligible for plagioclase within the analytical uncertainty of the <sup>87</sup>Sr/<sup>86</sup>Sr ratio, and that external normalization using the significantly better matrix matched standard Te-1 should provide accurate <sup>87</sup>Sr/<sup>86</sup>Sr ratios for these two plagioclase sample transects. Data reduction was carried out using an inhouse excel spreadsheet. A more detailed description of the in situ Sr isotope method used in this study is provided in Bevan et al. (2021).

### 3.4. Age Correction of <sup>87</sup>Sr/<sup>86</sup>Sr

Continued beta decay of <sup>87</sup>Rb may have led to ingrowth of the stable <sup>87</sup>Sr in plagioclase crystals and groundmass glasses long after the cooling of the ignimbrites, given their eruption ages of several million years. The static ion collection used to collect multiple SrF<sup>+</sup> isotopes in this method results in no Rb<sup>+</sup> ions being simultaneously collected during ablation. Rb-Sr analysis using Proteus is possible using a dynamic ion collection procedure. However, this compromises <sup>87</sup>Sr/<sup>86</sup>Sr ratio precision due to the inability to measure SrF<sup>+</sup> ions during Rb<sup>+</sup> collection and settling times between the required magnet jumps (Bevan et al., 2021). Therefore, to avoid the impact on <sup>87</sup>Sr/<sup>86</sup>Sr ratio precision, the significance of the effect of <sup>87</sup>Sr ingrowth in plagioclase, was evaluated using a subset of crystals from each of the studied eruptions. These crystals were analyzed for <sup>85</sup>Rb/<sup>88</sup>Sr using a Faraday cup collector array, equipped with 10<sup>11</sup> Ω feedback resistors, in a static measurement configuration. Measured <sup>85</sup>Rb/<sup>88</sup>Sr ratios were externally normalized to NIST SRM 610 (Bevan et al., 2021; Wise & Watters, 2012) to calculate the sample <sup>87</sup>Rb/<sup>86</sup>Sr ratio (Table S3 in Data Set S1). Using the age equation of the form:

$$\left(\frac{87\text{Sr}}{86\text{Sr}}\right)_{\text{initial}} = \left(\frac{87\text{Sr}}{86\text{Sr}}\right)_{\text{observed}} - \frac{87\text{Rb}}{86\text{Sr}} e^{((\lambda t)-1)},$$

where λ is 1.3972 × 10<sup>-11</sup> a<sup>-1</sup>, the decay constant of <sup>87</sup>Rb (Villa et al., 2015), and t is the age of the eruption (Salisbury et al., 2011). The calculations indicate that radiogenic ingrowth in plagioclase crystals of the

considered eruptions is smaller than the analytical uncertainty and is thus not considered further. All glass analyses presented in the manuscript have been corrected to initial values at the eruption age using the same approach. The difference between observed and initial  $^{87}\text{Sr}/^{86}\text{Sr}$ , resulting from radiogenic ingrowth in glasses, varied between 0.0003 and 0.0009.

### 3.5. Diffusion Modeling

To constrain the maximum timescales of plagioclase crystal residence we model the diffusive equilibration of Sr-isotopes in plagioclase at pre-eruptive magmatic temperatures. Diffusion coefficients for Sr equilibration in plagioclase have been determined experimentally by Cherniak and Watson (1994) for elemental (chemical) diffusion and by Giletti and Casserly (1994) using an isotopic tracer approach. We consider the latter experiments more applicable to model  $^{87}\text{Sr}/^{86}\text{Sr}$  diffusion in plagioclase, given the diffusion style, major element composition and temperature range ( $\text{An}_2\text{--An}_{96}$ ; 550–1300°C) of the experimental calibration. The Arrhenius equation for the tracer diffusion coefficient of Giletti and Casserly (1994) can be written as:

$$D = 2.92 \times 10^{-4.1X_{\text{An}}-4.08} \exp\left(\frac{-276000}{RT}\right),$$

where  $X_{\text{An}}$  is the molar fraction of anorthite in plagioclase,  $R$  is the ideal gas constant, and  $T$  is the temperature in Kelvin. To account for the spatial dependence of the diffusion coefficient along the  $X_{\text{An}}$  profile, we solve the one-dimensional diffusion equation of the form:

$$\frac{\partial C}{\partial t} = \frac{\partial}{\partial x} \left( D(x) \frac{\partial C}{\partial x} \right),$$

where  $C$  is  $^{87}\text{Sr}/^{86}\text{Sr}$ ,  $t$  is time in seconds, and  $x$  the spatial coordinate in meters. We use an explicit finite difference method to solve the diffusion equation numerically (Costa et al., 2008; Dohmen et al., 2017; Weber et al., 2019). As  $D$  is variable as a function of space, which is constrained by the  $X_{\text{An}}$  profile, it must be evaluated between numerical nodes to maintain accuracy of the solution. The discretized diffusion equation takes the form:

$$\frac{\partial}{\partial x} \left( D(x) \frac{\partial C}{\partial x} \right) \Big|_i = \frac{D_{i+\frac{1}{2}} \frac{C_{i+1} - C_i}{dx} - D_{i-\frac{1}{2}} \frac{C_i - C_{i-1}}{dx}}{dx},$$

where  $i$  is the index of the numerical node,  $dx$  is the spatial dimension of a numerical grid point. The An and Sr-isotope profile for each modeled crystal were interpolated to 700 numerical grid points using a cubic spline fit. The left boundary of the Sr-isotope profile, corresponding to the outermost rim in contact with melt, was fixed at its initial value throughout the simulation, thereby treating the melt as an infinite reservoir able to diffusively equilibrate with the crystal. In cases of contrasting outermost rim and glass compositions, we additionally ran simulations in which the outer boundary was set at the observed glass Sr-isotope ratio. A zero-flux boundary condition was employed at the end of profile in the interior of the crystal. Initial conditions in the diffusion modeling and used temperatures are discussed in Section 4.2.

## 4. Results

### 4.1. Textural and Geochemical Characterization

A total number of 45 crystals for the three studied eruptions that is, Atana:  $n = 14$ , Toconao:  $n = 19$ , and Tara:  $n = 12$ , have been imaged using back-scatter electrons (BSE) to reveal their chemical zonation pattern. A representative selection of the zoning types of these crystals is shown in Figure 2 and the full set of BSE images that were collected within the course of this study are available in the electronic supplementary materials. The imaged grains span a wide range of textural types but are typically subhedral in shape with faceted rims and partially broken faces along cleavage plains that may either be attributed to crushing during sample preparation but may also reflect explosive volcanic processes (Taddeucci et al., 2021; van Zalinge et al., 2018). Although the zoning is complex with multiple resorption and overgrowth horizons, the pattern in most crystals can be described as normal zoning with higher An (molar  $\text{Ca}/[\text{Ca} + \text{Na} + \text{K}]$ ) contents in the cores compared to overgrowth rims. Several common and distinct features are evident between samples from different eruptions. Atana plagioclases show the most severe zonation pattern with multiple dissolution horizons, patchy and sieve textures in crystal

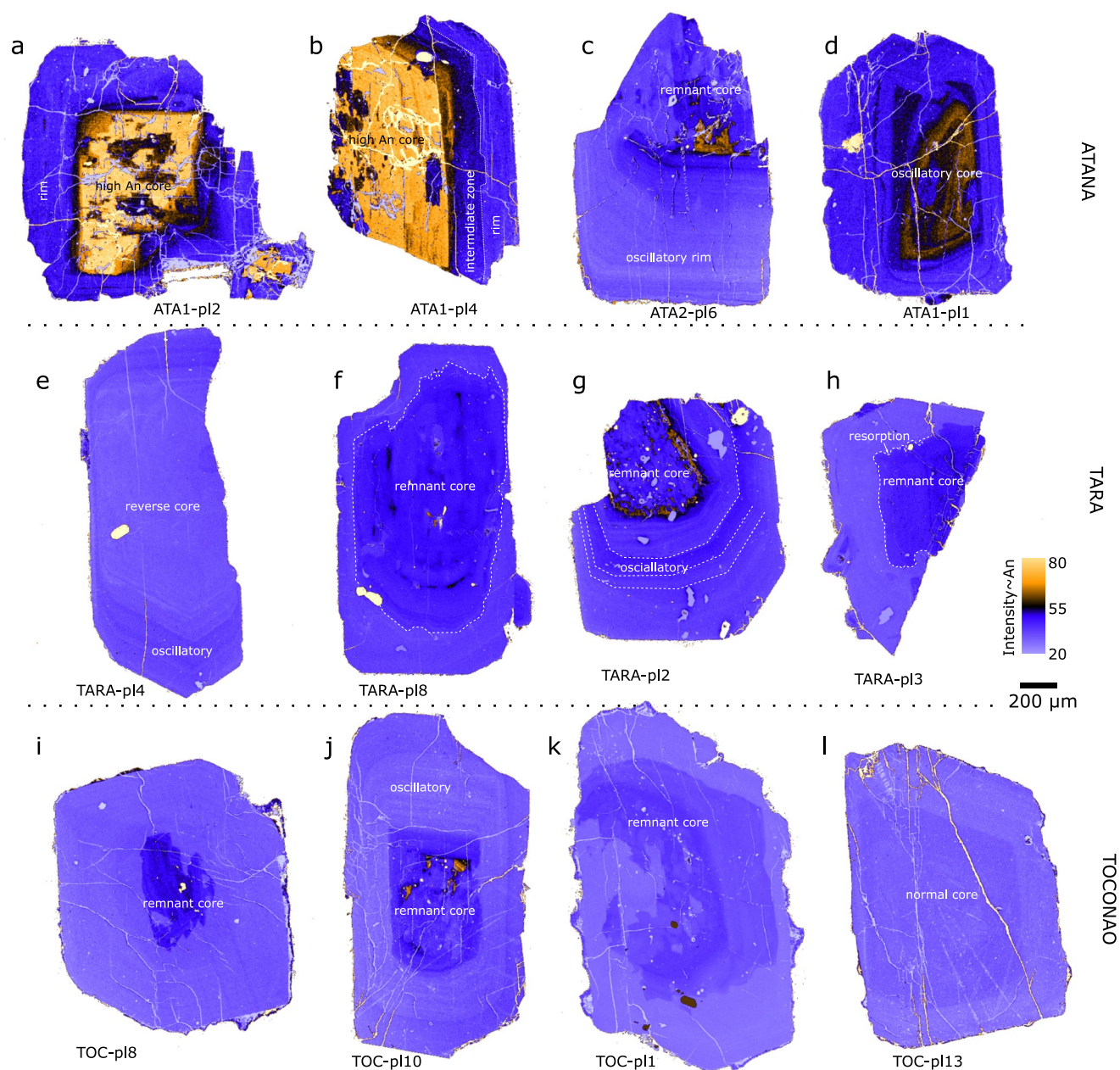


**Figure 2.** Back-scatter electron images of plagioclase crystals from the (a–d) Atana, (e–h) Tara, and (i–l) Toconao eruptions. Greyscale backscatter electron intensities were recolored to enhance the visibility of prominent zonation features using the software package ImageJ. The color scale is proportional to the major element composition of the crystals, with blue color tones corresponding to lower An-contents and yellow colors indicative of higher An contents in plagioclase.

cores that are present in 13 out of 14 imaged grains. Later stages of crystal growth prior to Atana eruption have resulted in oscillatory or multi-step rim formation of typically a few 100  $\mu\text{m}$  thickness and lower An contents. Boundaries between the described growth zones frequently show sudden shifts in BSE intensity, with or without the presence of resorption surfaces, indicating that the crystals have experienced drastic shifts in conditions during their growth history. Comparable zoning textures of relatively high An content in remnant crystal cores, although with less severe reaction textures, are observed in 10 out of 19 crystals from the Toconao eruption. Like Atana plagioclase, overgrowth rims in Toconao grains show weak oscillatory zoning that comprise the bulk of most grains. The described textures of Atana and Toconao plagioclase are similar to Tara grains, yet a distinct feature in the BSE images of the latter eruption is the presence of more pronounced resorption horizons in the interior of the crystals, resulting in greater amplitude of compositional oscillations. Such horizons are

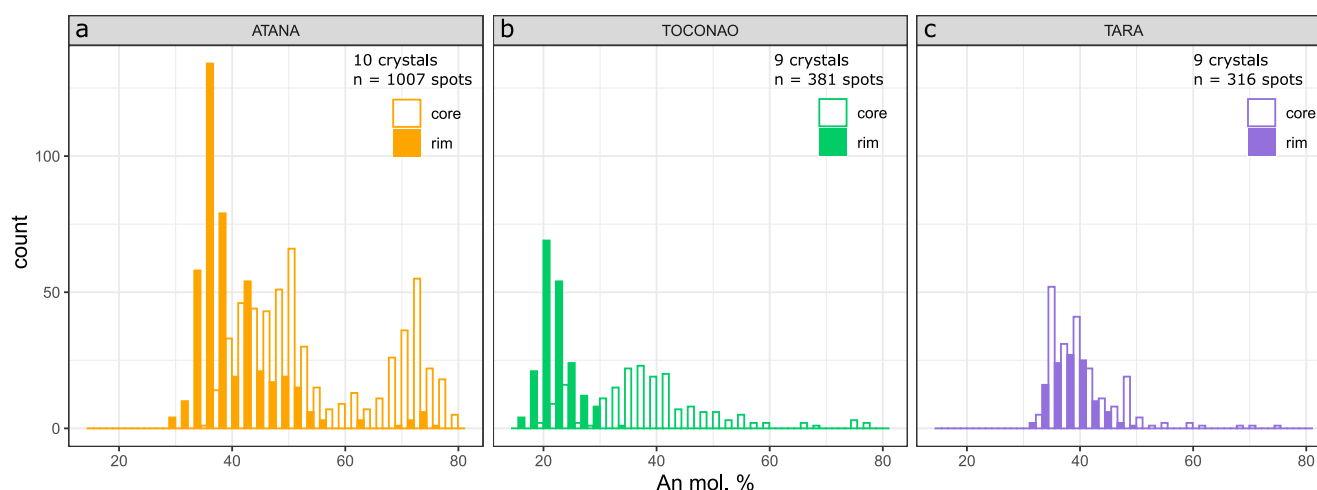


**Figure 3.** Histograms of molar anorthite contents of plagioclase crystals from the (a) Atana (orange), (b) Toconao (green), and (c) Tara (purple) ignimbrite. In each case, filled columns represent crystal rim compositions and unfilled columns are core compositions that have been assigned based zonation textures in BSE images. Atana and Toconao histograms show multi-modal distributions of rim and core compositions, while Tara samples are more restricted and unimodal.

present in 5 out of 12 grains at distances of 200–1,000  $\mu\text{m}$  from the crystal rim. The observed range of zonation types is consistent with previous work on Atana, Toconao and Tara plagioclase, based on a larger number of analyzed transects (Grocke, de Silva, Iriarte, et al., 2017; Grocke, de Silva, Wallace, et al., 2017; Lindsay, de Silva, et al., 2001; Lindsay, Schmitt, et al., 2001). We are therefore confident that the variation in crystal cores is representative of the studied eruptions even when considering that some cores may have not been exposed due to 2D sectioning effects. Taken together, the observed zonation patterns for the three eruptions are similar in that they record oscillatory overgrowth of compositionally distinct pre-existing grains but no evidence for large scale reheating of the system, which would be manifest in crystal rims as either pronounced resorption surfaces or reverse zonation with high BSE intensity (Cashman & Blundy, 2013; Humphreys et al., 2006; Ruprecht & Wörner, 2007; Weber et al., 2019).

To quantify the compositional variation in major and minor elements of plagioclase, 28 crystals (10 Atana, 9 Tara, and 9 Toconao) were chosen for EPMA analysis. Our data set comprises 1,704 spot analysis (Atana:  $n = 1,007$ , Tara:  $n = 316$ , Toconao:  $n = 381$ ), with spacing of 15–40  $\mu\text{m}$  between adjacent measurement spots for all grains, except for 8 Atana crystals that were measured with higher spatial resolution of 5–10  $\mu\text{m}$ . Molar anorthite (An) contents span a wide range of  $\text{An}_{29-80}$  for Atana,  $\text{An}_{30-76}$  for Tara, and  $\text{An}_{15-77}$  for the Toconao eruption (Figures 3a and 3b; Table S1 in Data Set S1). These findings expand the ranges of previously published plagioclase data, namely  $\text{An}_{35-49}$  for Atana and  $\text{An}_{12-30}$  for Toconao (Lindsay, Schmitt, et al., 2001). Plagioclase compositions of the Tara ignimbrite are constrained to vary between  $\text{An}_{30-76}$  (Figure 3c), expanding the previously reported range of  $\text{An}_{30-66}$  (Grocke, de Silva, Iriarte, et al., 2017). Both minor reverse and normal zonation patterns are evident (Figure 2), resulting in no systematic difference between crystal cores and rim compositions (Figure 3). Core-rim differences are, however, pronounced in the Atana and Toconao samples. Compositional distributions of An (mol.%) contents for the Atana and Toconao eruptions are bimodal, with prominent peaks between  $\text{An}_{35-42}$  for Atana and  $\text{An}_{20-23}$  for Toconao that correspond texturally to crystal rim compositions. Core compositions for Atana crystals are multi-modal with peaks between  $\text{An}_{40-55}$  in oscillatory zoned grains, and  $\text{An}_{65-80}$  in crystals with sieve or patchy zoned cores. Toconao plagioclase cores span a wide range ( $\text{An}_{20-80}$ ) but show a dominant peak between  $\text{An}_{30-50}$ , overlapping with the mode of Atana rim and oscillatory core compositions.

## 4.2. Crystal Sr-Isotope Stratigraphy

Plagioclase crystals from all three studied eruptions show considerable  $^{87}\text{Sr}/^{86}\text{Sr}$  zonation in core to rim traverses. The Sr isotopic composition in Atana crystals ranges from 0.7082 to 0.7123 (representative 2SE uncertainty:  $\pm 0.0002$ ; Table S2 in Data Set S1), which is significantly larger than the spread of 0.7094–0.7116 recorded by published bulk rock compositions (Lindsay, Schmitt, et al., 2001), but similar to the total  $^{87}\text{Sr}/^{86}\text{Sr}$  bulk-rock diversity of various ignimbrites across the wider APVC (Kay et al., 2010). Toconao plagioclases record



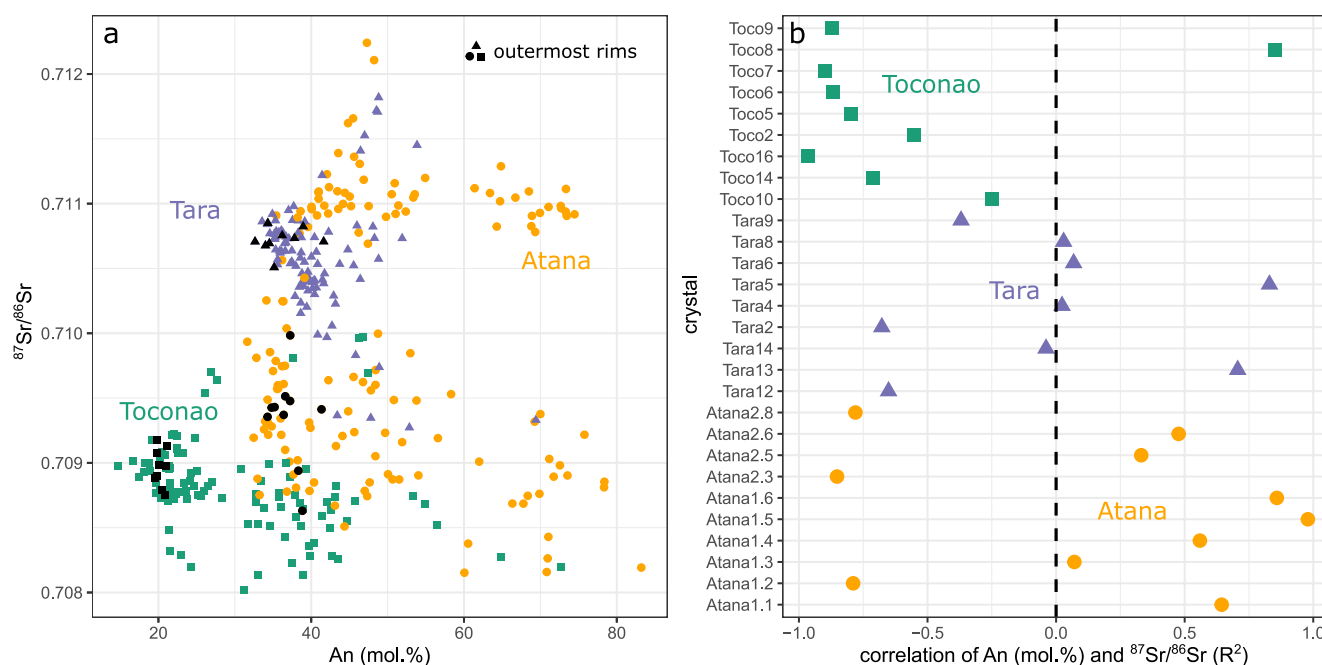


**Figure 4.** Relationship of An (mol.%) and  $^{87}\text{Sr}/^{86}\text{Sr}$  in plagioclase. (a) Anorthite (An—mol.%) versus  $^{87}\text{Sr}/^{86}\text{Sr}$  in plagioclase from the three studied ignimbrites. Color coding and symbols reflect the eruption: Atana (orange dots), Tara (purple triangles), and Toconao (green squares). Outermost rims in each eruption are shown with black symbols. (b) Correlation coefficient ( $R^2$ ) for An (mol.%) and  $^{87}\text{Sr}/^{86}\text{Sr}$  for each analyzed crystals, color coded for eruption as in (a).

Sr-isotopic compositions of 0.7080–0.7100, significantly lower compared to published values for Toconao bulk pumices of 0.7106–0.7131 (Lindsay, Schmitt, et al., 2001). Finally, Tara crystals range from 0.7093 to 0.7118, overlapping with the lower end of the range in published bulk-pumice analyses ( $^{87}\text{Sr}/^{86}\text{Sr} = 0.7094\text{--}0.7132$ ) for this eruption (Grocke, de, Silva, Wallace, et al., 2017). These differences likely reflect the limited number of crystals analyzed in this study, given the highly heterogeneous compositions of both crystals and bulk-rock analyses.

The relationship between An and  $^{87}\text{Sr}/^{86}\text{Sr}$  in plagioclase from the three studied eruptions is complex (Figure 4). In the case of the Atana eruption, a steep positive correlation of An and  $^{87}\text{Sr}/^{86}\text{Sr}$  is evident for crystals between  $\sim\text{An}_{30\text{--}50}$ , while higher An analyses branch off from this general relationship in two broad arrays around 0.7111 and 0.7080–0.7090 (Figure 4a). A somewhat simpler pattern is found for the Toconao and Tara eruptions. Both show no correlation between An and  $^{87}\text{Sr}/^{86}\text{Sr}$  when considering all analyses together but show data clusters around  $\text{An}_{20}$  and  $^{87}\text{Sr}/^{86}\text{Sr} \sim 0.7090$  for Toconao, and  $\text{An}_{35}$  and  $^{87}\text{Sr}/^{86}\text{Sr} \sim 0.7108$  for Tara, while higher An contents generally show a wider range of corresponding Sr-isotope ratios. Outermost crystal rim compositions record a common isotope ratio and An content of 0.7094–0.7095 ( $\sim\text{An}_{35}$ ) in 7 out of 10 crystals for the Atana eruption, 0.7088–0.7092 ( $\sim\text{An}_{20}$ ) for Toconao (9 out of 9 crystals), and 0.7105–0.7108 ( $\sim\text{An}_{35}$ ) for Tara plagioclase (9 out of 9 crystals).

On the level of individual crystals, different types of correlation between An and Sr isotopes can be observed (Figure 4b). Pearson's correlation coefficients ( $R^2$ ) for the Toconao eruption range from  $-0.97$  to  $0.85$  but are mostly negative (i.e., anti-correlation) with median  $R^2$  of  $-0.79$ . Correlation coefficients for Atana crystals are mostly positive but range between  $-0.85$  and  $0.98$ . Crystals from the Tara eruption show mostly no correlation between An and  $^{87}\text{Sr}/^{86}\text{Sr}$  ( $n = 4$ ), but also positive ( $n = 2$ ) and negative ( $n = 2$ )  $R^2$  between  $-0.68$  and  $0.83$ . However, we note that crystals that show good visual correspondence can result in low  $R^2$  given the different spatial resolution of An and isotopic measurements (cf., crystal Tara6 in Figures 4 and 6c).

## 5. Discussion

### 5.1. Geochemical Records of Eruptible Magma Assembly

Considering the close temporal and spatial association of the Toconao and Atana eruptions, and that the crystal-poor Toconao rhyolite may represent an extracted liquid from the larger crystal-rich dacitic reservoir

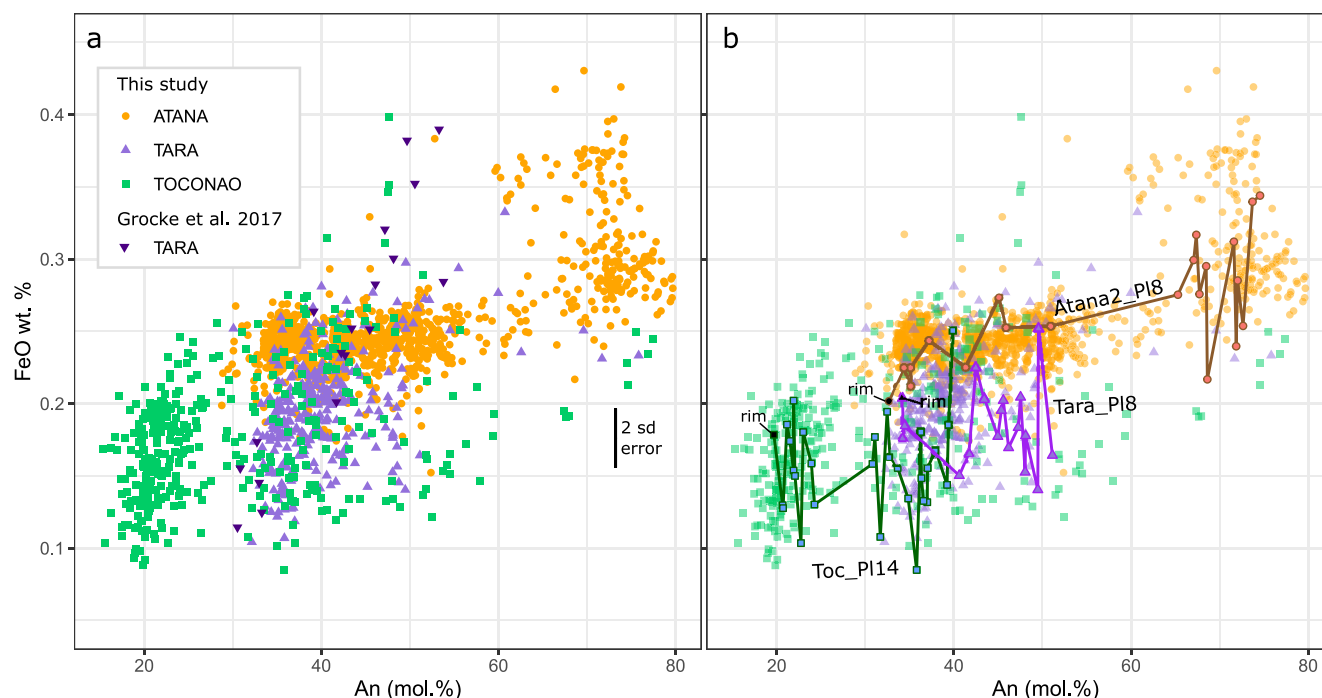


**Figure 5.** (a) Anorthite (An—mol.%) versus total FeO (wt.%) in plagioclase from the three studied ignimbrites. Color coding and symbols reflect the eruption: Atana (orange dots), Tara (purple triangles), and Toconao (green squares). Data for the Tara eruption from Grocke, de, Silva, Iriarte, et al. (2017) and Grocke, de, Silva, Wallace, et al. (2017) were filtered for analytical totals between 98.5 and 101.5 wt.% and are shown as inverted dark violet triangles. Published plagioclase FeO contents for the Atana and Toconao eruptions (Lindsay, Schmitt, et al., 2001) are reported to only one decimal place and are therefore not shown. (b) Sample data as in (a) but with plotted core-rim trajectory of a single crystal from each eruption.

that fed the Atana eruption (Lindsay, Schmitt, et al., 2001), a petrogenetic link between the overlapping crystal populations could be expected. However, FeO<sub>t</sub> contents of Atana plagioclase span a significantly narrower range of 0.23–0.25 wt.% (first to second quantile) at An<sub>30–50</sub> compared to Toconao plagioclase (FeO<sub>t</sub> = 0.15–0.23 wt.%; first to second quantile), indicating that the two eruptions have separate and distinct petrogenetic histories (Figure 5a), an observation borne out by the different outer-rim Sr isotope ratios of plagioclases from the two eruptions (Figure 4a).

The patterns of major and minor element zonation in plagioclase can be further used to gain insights into pre-eruptive magmatic conditions during crystallization. The transition from crystal cores to rims of most of the analyzed Atana, Toconao, and Tara plagioclases, show abrupt drops in An content on the order of 10–40 mol.% (Figures 5b and 6). These shifts in An may be associated with drops or increases on the order of 0.05–0.2 wt. % FeO, but in some cases FeO remains invariant with respect to An (Figures 5b and 6). Petrological experiments show that the An content is positively correlated with temperature,  $p\text{H}_2\text{O}$  and more mafic melt chemistry (Cashman & Blundy, 2013), whereas FeO is mostly sensitive to  $f\text{O}_2$  and the Fe content of the melt (Wilke & Behrens, 1999). Anorthite-dependent partitioning calculations (Bindeman et al., 1998) using a range of bulk-rock, melt inclusion and groundmass compositions for the three studied eruptions indicate a strong melt chemical control for grains showing large core to rim chemical variation. These calculations do not account for the  $f\text{O}_2$  dependence of Fe partitioning in plagioclase, but a comparison of predicted partition coefficients using the Bindeman et al. (1998) model and the experiments of Wilke and Behrens (1999) show good agreement at  $f\text{O}_2$  values relevant for the three eruptions considered here ( $\Delta\text{NNO} +1$  to  $+2$ ; Grocke, de, Silva, Iriarte, et al., 2017; Grocke, de, Silva, Wallace, et al., 2017; Lindsay, de Silva, et al., 2001; Lindsay, Schmitt, et al., 2001; Figure S2 in Supporting Information S1). High An cores ( $\sim\text{An}_{60–80}$ ) in Atana samples are consistent with crystallization from liquids similar to the bulk-rock dacite and minor andesite inclusions (Figure 7a), while more evolved Toconao ( $\sim\text{An}_{30–50}$ ) and Tara ( $\sim\text{An}_{30–50}$ ) cores reflect growth from mostly rhyolitic melts (Figures 7b and 7c). While this is in line with a strong melt chemical control on the observed compositional variation, the shift in An content without co-variation in FeO that is observed in several crystals of each eruption (Figures 6b and 6d–6f) is more consistent with a change in pre-eruptive  $p\text{H}_2\text{O}$ . Additionally, in some crystals FeO and An contents,

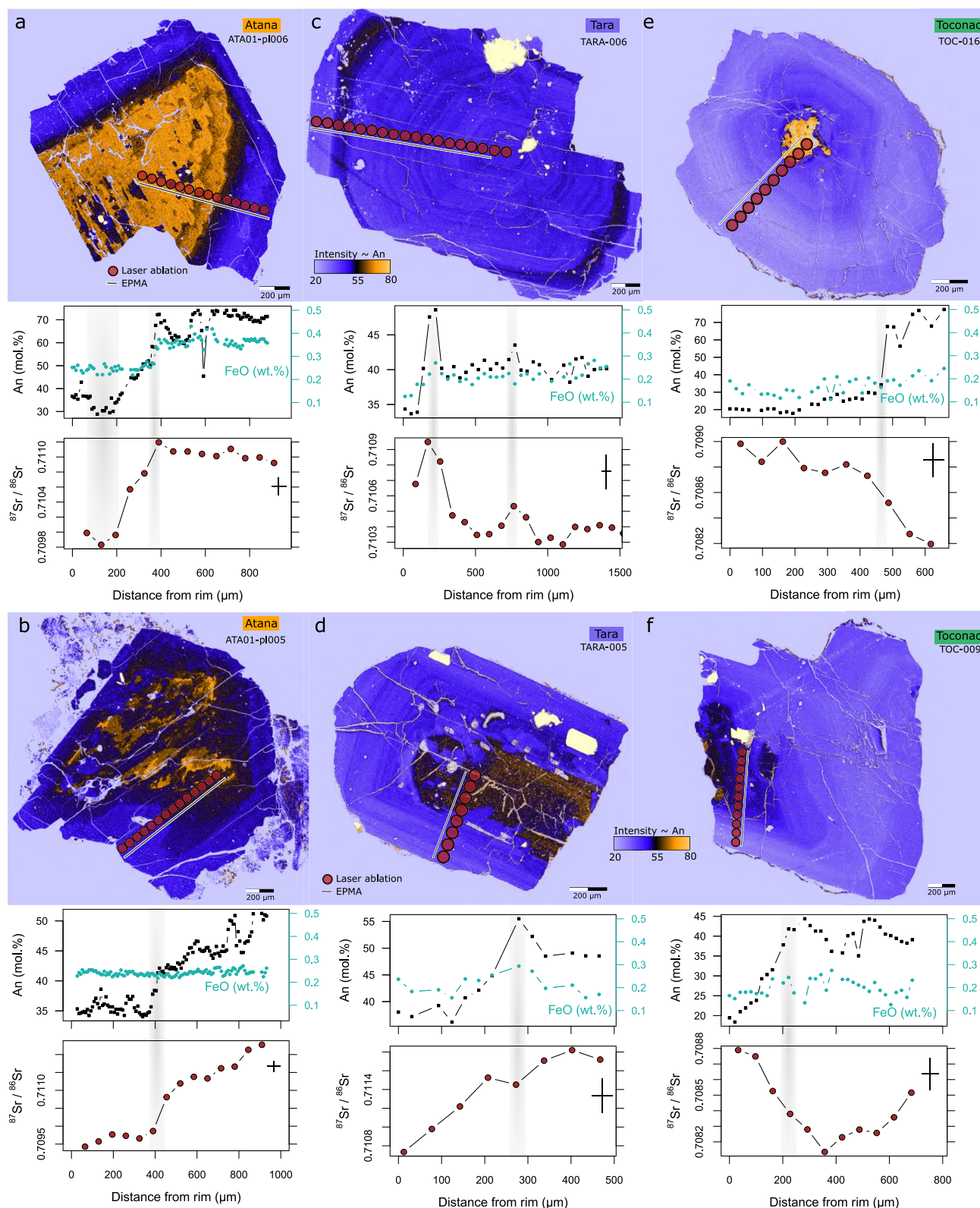


**Figure 6.** Profiles of analytical traverses (EPMA: black lines; LA-MC-ICP-MS: red spots) through selected plagioclase crystals are shown on BSE images. Greyscale intensity of the BSE images was color coded for An content. Major and minor elemental zonation traverses (An: black squares; FeO: turquoise dots) and  $^{87}\text{Sr}/^{86}\text{Sr}$  are shown for each crystal versus distance from the outermost crystal rim ( $\mu\text{m}$ ). Black shaded areas indicate correspondence between EPMA and isotope traverses. (a–b) Atana crystals, (c–d) Plagioclase from the Tara eruption, and (e–f) crystals from the Toconao ignimbrite. Representative error bars (2SE) and spatial resolution are shown for each isotope profile as black cross.



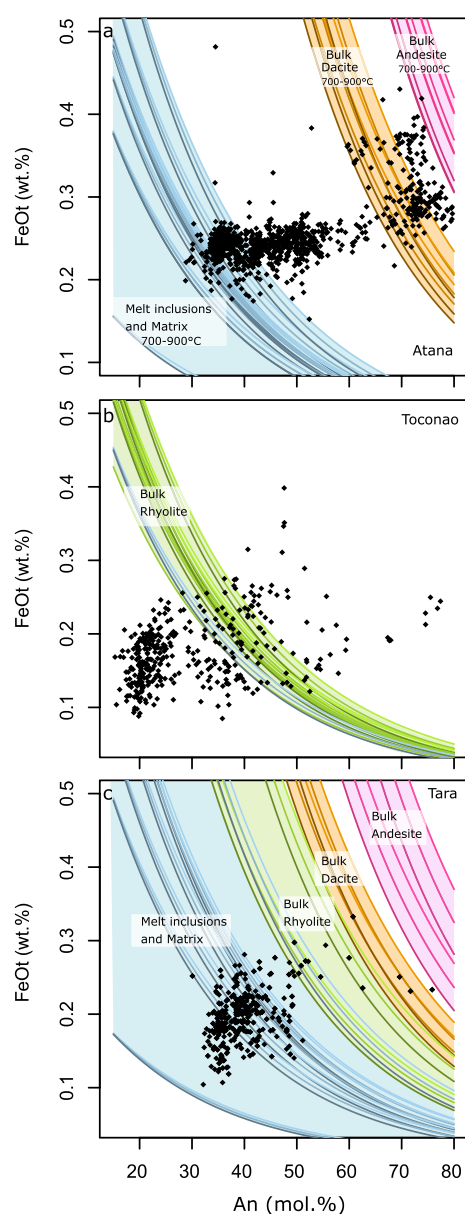


**Figure 7.** Molar fraction of anorthite ( $X_{an}$ ) versus  $FeO_t$  (wt.%) for all plagioclase crystals from the three studied eruptions (a) Atana, (b) Toconao, and (c) Tara. Colored lines in each plot show equilibrium partitioning of FeO in plagioclase for a range of bulk-rock and glass compositions for each of the eruptions (Grocke, de, Silva, Wallace, et al., 2017; Lindsay, Schmitt, et al., 2001) in the temperature range 700 (colored darker lines) to 900°C (brighter lines) using the An-dependent partitioning relations of Bindeman et al. (1998). Melt inclusion and groundmass glasses are shown as blue, bulk-rhyolites as green, bulk-dacite as orange, and bulk-andesite as pink lines.

of the ignimbrites (Figure 8; Tables S2 and S4 in Data Set S1), showing that the final stage of plagioclase growth reflects crystallization from the carrier melt of the eruptible magma that fed each eruption. Tara glass  $^{87}Sr/^{86}Sr$  ratios are, on average, lower compared to the outermost crystal rim compositions, but mostly in agreement within measurement uncertainty. As the Sr isotope ratio in plagioclase records the melt isotopic composition at time of growth, which may later be modified by diffusive re-equilibration, this convergence of  $^{87}Sr/^{86}Sr$  documents a drastic change in melt chemistry prior to each eruption. More importantly, the more homogeneous isotope

show a linear increase toward the outermost rim (Figures 6a, 6b, 6d, and 6e), which could indicate progressive heating of a mush reservoir. We test the significance of this hypothesis by using two plagioclase-liquid models to translate increasing An contents into temperature changes (Putirka, 2005; Waters & Lange, 2015). Using a fixed melt  $H_2O$  content of either 4 or 7 wt.%, total pressure between 200 and 400 MPa, and the Atana groundmass glass composition (Lindsay, Schmitt, et al., 2001), the observed linear increase in An content of 10 mol.% can be translated into about 10–20°C temperature increase. Based on water-saturated experiments for dacite bulk-rock compositions at 200 MPa and temperatures <800°C (Caricchi & Blundy, 2015), temperature change of 10–20°C would translate into a melt fraction change of about 10%, which in isolation is unlikely to have generated the eruptible magma in the case of the Atana eruption. In summary, the An-FeO systematics of plagioclase indicate a wide variety of different histories for individual crystals that experienced changes in melt chemistry and  $pH_2O$  during their growth.

Similar to An-FeO variation, the differences in observed correlation between An and  $^{87}Sr/^{86}Sr$  (Figure 4) suggest multiple pathways in magma chemistry leading up to each of the three eruptions. Generally, the tendency of silicic magmas to show higher degrees of crustal contamination compared to more mafic melts, leads to a negative correlation of An content and  $^{87}Sr/^{86}Sr$  in plagioclase that has been well documented at several volcanic systems (e.g., Davidson et al., 2001, 2007; Ramos et al., 2005; Tepley et al., 2000). In the case of the large-volume eruptions considered here, a more complex relationship is evident, showing negative, positive and no obvious correlation between An and  $^{87}Sr/^{86}Sr$  (Figures 4 and 6). However, this deviation from the expected behavior is not surprising when considering that, on the basis of zircon geochronology, each eruption was preceded by a protracted history of mush accumulation over about 1 million years (Kern et al., 2016), and that bulk-rock  $^{87}Sr/^{86}Sr$  of Central Andean magmas are highly variable, even for the same eruption in some cases (Brandmeier & Wörner, 2016; Grocke, de Silva, Iriarte, et al., 2017; Grocke, de Silva, Wallace, et al., 2017; Lindsay, de Silva, et al., 2001; Lindsay, Schmitt, et al., 2001). It is therefore likely that the pre-eruptive mush system contained a plexus of evolved melts with highly variable crustal  $^{87}Sr/^{86}Sr$  signature rather than binary low  $^{87}Sr/^{86}Sr$  (mafic) and high  $^{87}Sr/^{86}Sr$  (silicic) endmembers. Thus, both positive and negative correlations between An and  $^{87}Sr/^{86}Sr$  may come about through hybridization of variably contaminated melts. Differences in the fractions of crystals showing either type of correlation may represent a sampling bias or relate to the subset of melts that have contributed to the particular crystal population.

As shown in Figure 8, Sr-isotope profiles for each of the three eruptions show a common and systematic pattern of high isotopic diversity in crystal cores, evolving in strong gradients toward crystal rims that clearly show less isotopic variability compared to the interiors. These substantial variations in  $^{87}Sr/^{86}Sr$  ratio in core to rim traverses, reflect changes in melt isotopic composition in the runup to these events. The  $^{87}Sr/^{86}Sr$  ratios of outermost crystal rims for Atana and Toconao plagioclase coincides with the matrix glass composition



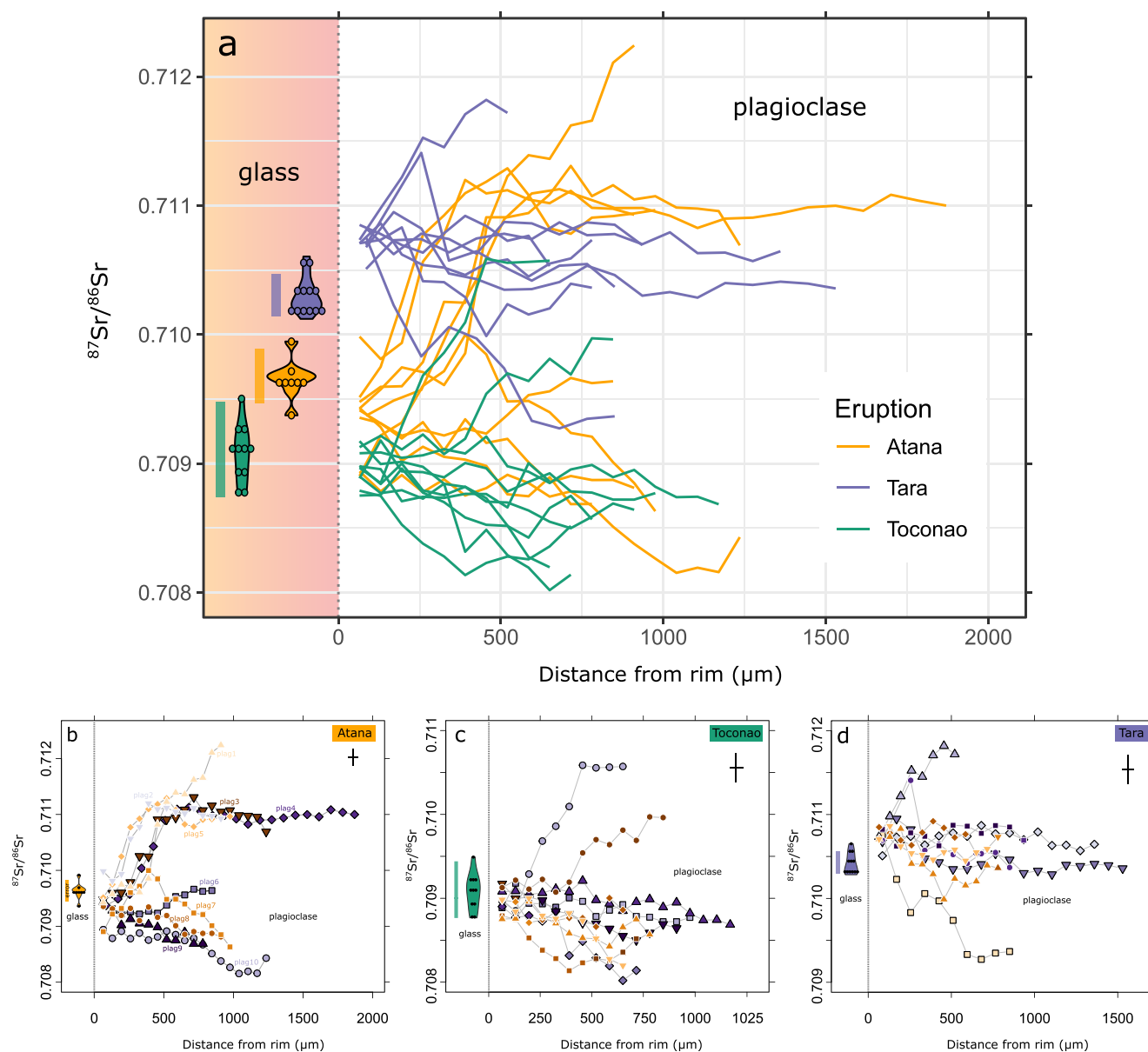


**Figure 8.** Sr isotopic traverses through plagioclase and groundmass glass compositions for the three studied eruptions (Atana: orange, Tara: purple, Toconao: green). (a)  $^{87}\text{Sr}/^{86}\text{Sr}$  analyses of glasses are shown as two-sided kernel density distributions (violin plots) in the shaded area. Vertical bars represent analytical uncertainties for a single groundmass spot analysis (2SE). The lines show analytical traverses as a function of distance from the crystal rim for all crystals, color coded for the different eruptions. Panels (b–d) are close-up views for the Atana, Toconao, and Tara eruptions respectively. Symbols and colors reflect different crystals; spot size and analytical uncertainty are indicated as a cross on the upper right side of each panel. Representative 2SE uncertainties for the isotope measurements are  $\pm 0.0002$ .

ratio toward the rim of crystals suggests that the final eruptible magma that fed the three eruptions emerged by incorporation of multiple distinct crystal populations, which must have developed separately in space and/or time, each of them undergoing their own distinctive evolution during growth from melt together with variable degrees of crustal contamination. The observation that Atana crystals show a larger fraction of heterogeneous cores compared to the Toconao and Tara samples (Figure 8) may relate to the larger interaction volume between incoming melt and heterogeneous crystal populations, given the larger size of the Atana eruption (1,800 km<sup>3</sup>; Lindsay, de Silva, et al., 2001) compared to Tara and Toconao (800 and 180 km<sup>3</sup> respectively; Lindsay, de Silva, et al., 2001; Grocke, de Silva, Iriarte, et al., 2017).

The processes that led to the amalgamation of the isotopically diverse crystal population prior to the Atana, Toconao and Tara eruptions can be further understood by tracing the evolution of  $^{87}\text{Sr}/^{86}\text{Sr}$  and FeO in the melt.

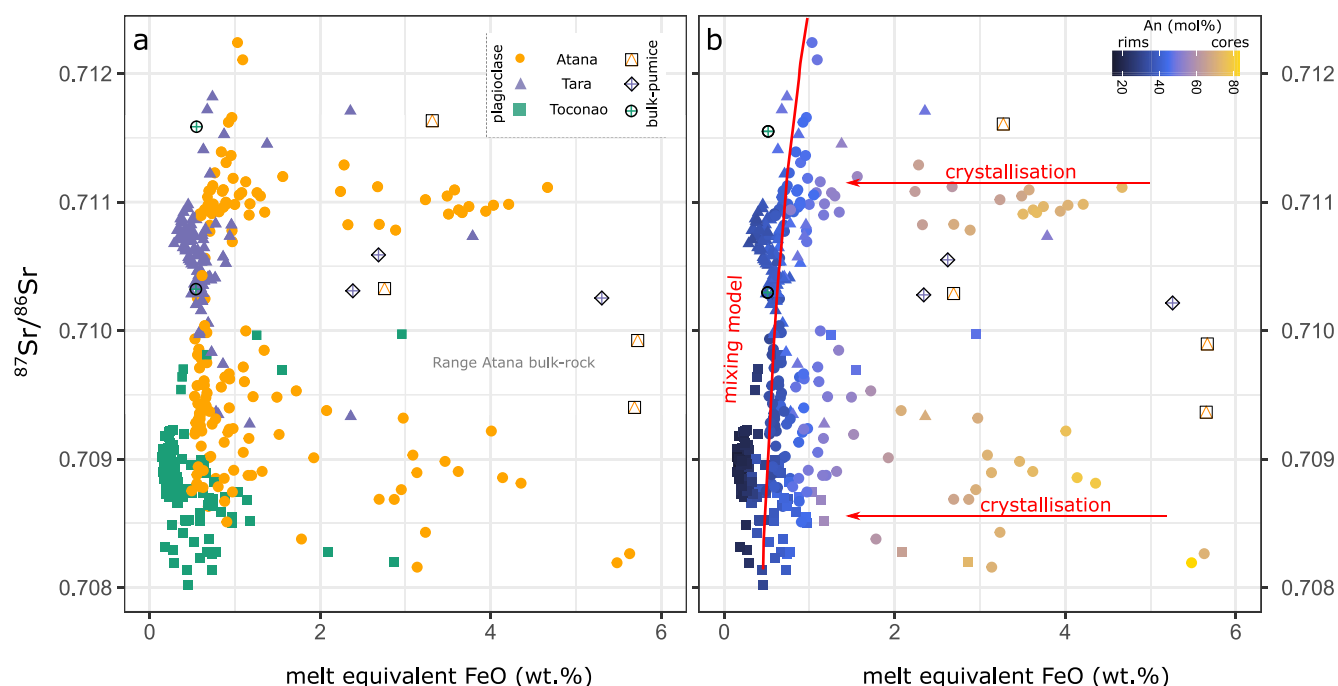


**Figure 9.** Melt equivalent FeO (wt.%) content vs.  $^{87}\text{Sr}/^{86}\text{Sr}$  of plagioclase. (a) Orange dots represent Atana, purple crosses Tara and green squares Toconao samples. The range of bulk-rock compositions for the Atana eruption is shown as gray shaded area. (b) Symbols are the same as in (a) but color coding reflects the molar An content of plagioclase. The red arrows illustrate the trajectory during crystallization at a specific Sr isotope composition. The red line is a steep mixing hyperbola between evolved melts with different  $^{87}\text{Sr}/^{86}\text{Sr}$  and FeO.

Using An-dependent partitioning relations (Bindeman et al., 1998), we invert plagioclase FeO contents into equivalent melt concentrations (Figure 9) and link the melt evolution to textural features observed in BSE images (Figure 6). High An crystal cores show melt equivalent FeO contents between 1.2 and 4.9 wt. %, consistent with their derivation from evolved andesite or dacite melts and depletion of FeO contents during crystallization processes due to co-precipitation of ferromagnesian phases and/or Fe-Ti oxides. The Sr-isotopic composition of high An cores vary between 0.7082 and 0.7111 with several trajectories of FeO depletion at different  $^{87}\text{Sr}/^{86}\text{Sr}$ , indicating that crystallization of individual magma aliquots that led to the formation of these cores occurred from a wide range of melts with variable degrees of crustal contamination. In contrast, rim compositions show melt equivalent FeO contents of mostly below 1 wt.%, implying that they grew from rhyolitic melt compositions. While FeO contents of the melts during crystallization of crystal mantles and, in particular, rims have been restricted, Sr-isotope compositions of plagioclase, which reflect the melt composition, show large variation. Such changes are inconsistent with simple crystallization or crustal assimilation scenarios but can be explained by progressive convergence of Sr isotopes in mixing/mingling processes of diverse crystal-rich magma pockets and/or disintegration of solid residue by an invasive rhyolite melt of different  $^{87}\text{Sr}/^{86}\text{Sr}$  composition for the three cases. Our data do not permit to estimate mixing/mingling endmembers or proportions, but the incoming melt may have merged a larger number of isotopically distinct crystal populations, which permits the definition of simple binary endmembers using a mixing hyperbola (Figure 9b). In summary, the isotopic and geochemical systematics of Atana, Toconao, and Tara plagioclase crystals record a late-stage convergence related to mixing/mingling of a rhyolite melt and diverse crystal populations without evidence for large-scale heating or mush defrosting. This hybridization process must therefore be related to an increase in melt fraction at relatively low pre-eruptive temperature.

## 5.2. Timescales of Eruptible Magma Residence

The strong Sr-isotope zonation gradients in plagioclase allows us to reconstruct the maximum time that the crystals could have resided in the final assembled eruptible magma by means of diffusion chronometry. As described above, amalgamation of the eruptible magma is recorded by plagioclase crystals as a convergence process, creating a common isotopic composition in most crystal rims, while retaining much larger diversity in crystal cores.

The isotopic disequilibrium between cores and rims, which were in local isotopic equilibrium with the carrier melt shortly prior to eruption, induces a chemical potential gradient that acted as a driving force for diffusive partial re-equilibration of Sr isotopes. This kinetic process is mostly dependent on the shape and magnitude of the gradient, and on temperature as an activation energy barrier that must be overcome for  $^{87}\text{Sr}$  and  $^{86}\text{Sr}$  isotopes to move to new sites in the crystal lattice. Pre-eruptive temperatures for the Atana ignimbrite have been estimated to vary between 750 and 790°C (Lindsay, Schmitt, et al., 2001) based on amphibole-plagioclase thermometry (Holland & Blundy, 1994), Fe-Ti oxide equilibration (Andersen et al., 1993), and two-feldspar thermometry (Ghiorso, 1984). Given that updated calibrations of the Fe-Ti oxythermometer have been published, it is worth revisiting the pre-eruptive temperature estimates for the Atana ignimbrite. Using the touching titanomagnetite-ilmenite pair compositions presented in Lindsay, Schmitt, et al. (2001) in conjunction with the oxide geothermometer of Ghiorso and Evans (2008) yields median temperatures of 754°C, lower than previous estimates, but in good agreement with estimates from amphibole-plagioclase temperatures (Holland & Blundy, 1994; Figure S3 in Supporting Information S1). Given the match of different independent thermometers and accounting for uncertainty of the estimates, we use a temperature of  $754 \pm 30^\circ\text{C}$  in subsequent diffusion calculations for the Atana ignimbrite. Temperature estimates for the Toconao eruption based on the two-feldspar thermometry are more limited but also indicate a temperature of 754°C, which given the uncertainty of the method ( $\pm 30^\circ\text{C}$ ) agrees well with previous estimates (730–750°C; Lindsay, Schmitt, et al., 2001). We therefore explore the same range of temperatures as for Atana in diffusion calculations for Toconao (i.e., 724, 754, and 784°C). Pre-eruptive temperatures of the Tara magma have been constrained based on amphibole-plagioclase pairs (Holland & Blundy, 1994) and touching Fe-Ti oxides (Ghiorso & Evans, 2008) and are in good agreement with each other (Groccke, de, Silva, Wallace, et al., 2017). Tara diffusion calculations were carried out using the median temperature of these estimates of 852°C and uncertainty of  $\pm 30^\circ\text{C}$ .

Before diffusion timescales can be reconstructed from the zonation profiles, initial conditions need to be evaluated, which is best achieved by comparing the systematics of elements with contrasting diffusive mobilities. Interdiffusion of CaAl–NaSi in plagioclase has been shown experimentally to be very slow even at much higher magmatic temperatures (M. Liu & Yund, 1992) than those considered here. Strontium isotopic tracer diffusion in plagioclase is, based on experiments (Giletti & Casserly, 1994), several orders of magnitude faster than CaAl–NaSi exchange, which implies that while An gradients remain stationary during protracted magma storage, Sr isotope profiles should undergo diffusive re-equilibration. Comparing the zoning pattern of An and  $^{87}\text{Sr}/^{86}\text{Sr}$ , we note that even though the resolution of EPMA ( $\sim 2\ \mu\text{m}$ ) and Proteus spots ( $\sim 80\ \mu\text{m}$ ) is very different, the profiles show a strong resemblance, typified by corresponding major gradients (Figure 6) and in some cases even minor features (Figures 6a and 6b). A decoupled evolution of An content and Sr isotopes is observed in several grains, which may reflect a different history compared to the other crystals without the development of strong isotopic gradients or partial diffusive equilibration. The latter is, however, difficult to reconcile with the observed profile shapes, if the original isotopic profile shape showed similar coupling of An and  $^{87}\text{Sr}/^{86}\text{Sr}$  as measured in the other crystals. Taken together, gradients and profile shapes indicate that the initial isotopic zoning patterns have not been modified drastically by diffusion but are mostly original crystal growth features, reflecting the isotopic composition of the melt. Any diffusion would only serve to smooth out the observed isotopic profiles.

The observation that Sr isotope profiles mostly reflect growth zoning rather than diffusive equilibration can be used to evaluate scenarios of eruptible magma residence, as diffusion at pre-eruptive temperatures would have flattened and smoothed the observed gradients. As we cannot rule out that pre-eruptive diffusion has occurred, we focus here on three scenarios, assuming that the magma equilibrated with a melt composition similar to the common rim observed in each case for the great majority of crystals (Figure 8). The first scenario (Scenario 0; Figure 10a) represents a case in which the observed profile is considered to represent only growth zoning, in which case we can track the maximum time that the profile could have survived equilibration with the common rim composition before it diffuses out of the error margins given by the analytical uncertainty. We refer to these as “survival timescales.” Survival timescales calculated using this approach for the Atana eruption ( $n = 7$ ; Figure 11; Table S5 in Data Set S1) span a wide range from 82 years to 23.8 ka, with most crystals recording maximum survival times of less than 1000 years (median: 513 years). Modeled Tara crystals ( $n = 6$ ) yield the shortest maximum residence times ranging from 24 to 1986 years with a median of 137 years; Toconao plagioclase ( $n = 4$ ) could have resided in the eruptible magma for more than 977 years on average (range 301–5815 years). These estimates include crystals that do not show large gradients in  $^{87}\text{Sr}/^{86}\text{Sr}$  yielding maximal timescales of several millennia. Most profiles for the Atana and Tara eruptions show survival timescales on the order of several

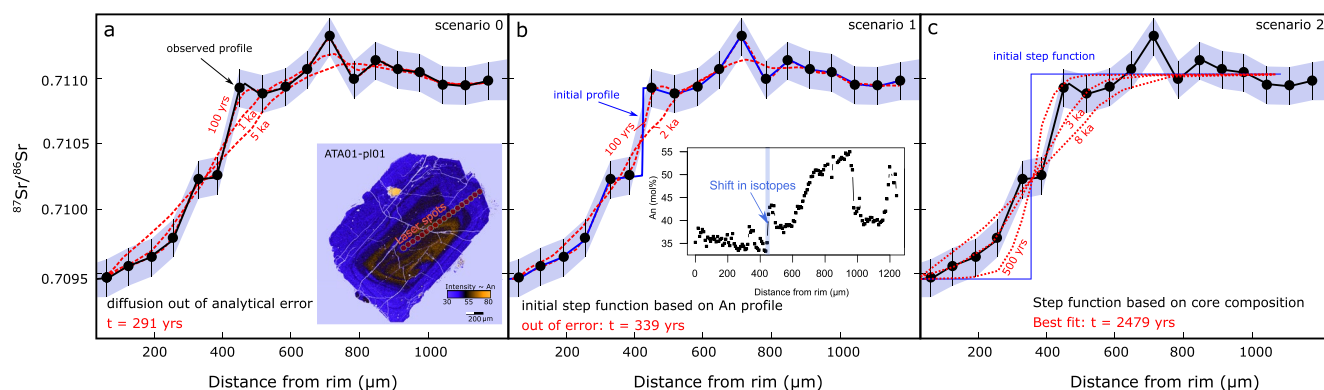


**Figure 10.** Illustration of different approaches to diffusion chronometry based on Atana crystal (ATA01-p11). (a) In scenario 0, the observed  $^{87}\text{Sr}/^{86}\text{Sr}$  isotope profile is taken to be the initial profile and the time is tracked for diffusion out of analytical uncertainty. Red dashed curves show modification of the observed (initial) profile after 100 years, 1 and 5 ka of diffusive equilibration. (b) Scenario 1: Based on a shift in An content (shown in the inset), the initial profile (blue line) is considered to be a step function. Red dashed curves illustrate the diffusive equilibration of the profile after 100 and 2000 years. (c) Scenario 2 represents a case where the initial profile (blue curve) is assumed to be a step function over the entire observed gradient. Results of diffusion modeling after 0.5, 3, and 8 ka are shown as red dashed curves.

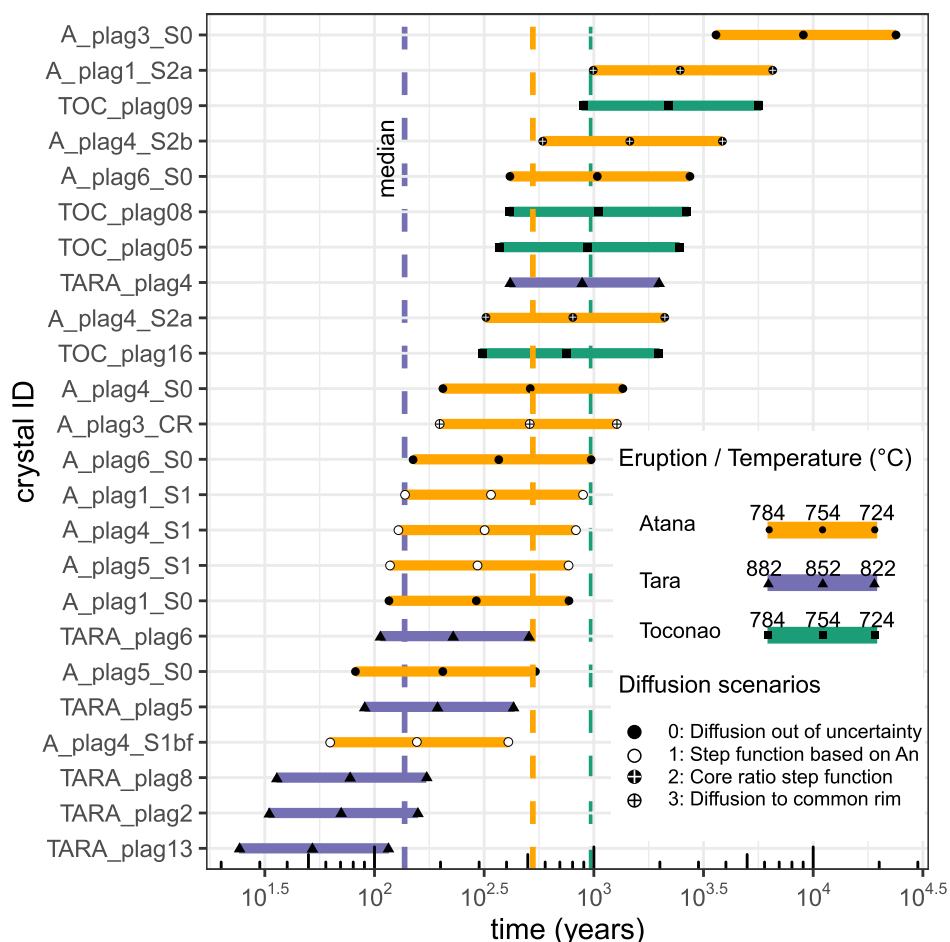


**Figure 11.** Summary of calculated diffusion timescales. Results are shown as log-scale ranked order plots of time in years for different crystals, with colors corresponding to the eruption: Atana (orange), Tara (purple), Toconao (green). Three timescales are shown for each crystal reflecting the range of investigated temperatures. Symbols indicate the diffusion scenario on which the timescales are based: black circles correspond to scenario 0 (diffusion out of analytical error); open circles to scenario 1 (step function based on An content); white cross to scenario 2 (Core ratio step function); and black cross to scenario 3 (diffusion to common rim). Dashed lines are medians of all diffusion estimates for the three eruptions.



decades to centuries, suggesting that the assembled eruptible magma has not existed in the crust for the protracted periods of time suggested by zircon geochronology (i.e., hundreds of thousands of years or more).

$^{87}\text{Sr}/^{86}\text{Sr}$  profiles may have been initially steeper than the observed profile and then relaxed diffusively to their observed gradients. We refer to these as “relaxation timescales.” To estimate the impact of different initial conditions on the calculated maximum residence timescale, we carried out diffusion calculations in two additional scenarios (Figures 10b and 10c). In Scenario 1, the initial profile shape is based on that of the An profile in those cases where the gradient in Sr-isotopes is correlated with a sharp drop in An content (Figure 10b), indicating that both features can be ascribed to a common process. This criterion is only met for three crystals from the Atana eruption, yielding timescales which are ~50–100 years longer than the corresponding survival timescales. Additionally, where possible, a best-fit time was calculated for the observed profile of one crystal (Atana plag3\_CR; Figure 11), indicating a maximum residence timescale of 156 years at 754°C. Alternatively (Scenario 2), the initial Sr isotope profile may have taken the form of a step function across the entire length of the observed gradient (Figure 10c), which results in timescales of 321–6556 years before diffusion would adjust the pattern to a shape similar to the observed profile within the analytical precision and spatial resolution of our measurements. However, we note that there is (a) no indication based on the An profile that such initial conditions are realistic and (b) that it is difficult to fit the observed profile from an initial step function spanning the entire gradient. We therefore suggest that calculation results of Scenarios 0 and 1, rather than Scenario 2, are more robust estimates of the maximum time that the crystals could have spent in the pre-eruptive magma.

While the convergence of  $^{87}\text{Sr}/^{86}\text{Sr}$  isotopic compositions toward a common outermost rim of 0.7095 is recorded in most crystals of the Atana eruption, some feldspars show different rim compositions (Figure 8a). This heterogeneity may be attributed to various effects, including the size of laser spots compared to outermost rim width of crystals, heterogeneous isotope composition of the melt and/or entrainment of the crystals shortly prior to eruption with insufficient time for re-equilibration. Although, Sr-isotope heterogeneity may to some extent be possible within the error margins of our glass analyses, and natural variability has been documented for other dacitic large-volume eruptions (Fish Canyon Tuff; Charlier et al., 2007), the variability in glass compositions is too small to explain these differences. In either case, Sr diffusion in melts is several orders of magnitude faster than in plagioclase feldspar (Perez & Dunn, 1996), which implies that differences in melt composition can only be preserved if they are created very shortly prior to eruption or if the eruptible magma assembly process and eruption initiation are contemporaneous. Our modeling indicates that entrainment of crystals with rim composition of 0.7086 could retain their chemical zoning for no more than 492 years at 754°C (197 years at 784°C; 1301 years at 724°C) if immersed in a melt in equilibrium with the common rim composition of 0.7095 for the Atana eruption (scenario 3; Figure 11).

In summary, survival, and relaxation timescales of Sr isotope gradients in Atana and Tara plagioclase indicate that most crystals could not have spent more than several decades to centuries in the assembled eruptible magma even when considering a conservative error margin of  $\pm 30^\circ\text{C}$  on the pre-eruptive temperature estimate. Toconao plagioclases indicate longer maximum residence timescales on the order of millennia. Although these timescales provide valuable insights into the upper time limit over which the eruptible magma existed in the crust prior to eruption, they also require that the growth and destabilization process resulting in the accumulation and evacuation of large-volume eruptible magma must operate on even shorter timescales.

### 5.3. Growth and Destabilization of Rhyolitic Melt Lenses

Field and petrological studies have shown that large-magnitude silicic eruptions constitute a dichotomy in physico-chemical conditions of magma bodies, exemplified by crystal-poor rhyolites (e.g., Toconao ignimbrite) and crystal-rich dacites (or monotonous intermediates; e.g., Atana ignimbrite). Over the last decades, broad consensus has emerged in the interpretation that monotonous intermediate magmas represent erupted crystal mushes that have experienced an increase in melt fraction prior to eruption, and that crystal-poor rhyolites originate through extraction of interstitial melt and gas from larger mush-dominated reservoirs that embody the source of monotonous intermediates (Bachmann & Bergantz, 2004; Bachmann & Huber, 2019; Cashman et al., 2017; Edmonds et al., 2019; Sparks et al., 2019). Various melt segregation mechanisms for the origin of rhyolitic melt lenses have been proposed, such as gas-driven filter pressing (Bachmann & Bergantz, 2006; Pistone et al., 2017; Sisson & Bacon, 1999), percolative reactive flow (Jackson et al., 2018; Solano et al., 2012, 2014), hindered settling or compaction-driven melt extraction (Bachmann & Bergantz, 2004; Hartung et al., 2019; Lee

et al., 2015; McKenzie, 1985), operating over a wide variety of timescales ranging from days to hundreds of thousands of years (Edmonds et al., 2019). Our Sr-isotope diffusion results for the Toconao eruption, an exemplar of crystal-poor rhyolite, constrains the maximum timescale for the accumulation and destabilization of the melt lens prior to eruption to be on the order several centuries to millennia. This requires relatively fast melt extraction and accumulation, consistent with models of porous reactive flow in crystal mushes (Jackson et al., 2018), but also requires relatively large crystal sizes and water-rich magma in compaction-driven and hindered settling extraction scenarios (Hartung et al., 2019). Moreover, our finding of an isotopically distinct melt composition, and more variable FeO contents in plagioclase for the Toconao eruption, suggest that this rhyolite does not simply represent an extracted differentiated liquid from the mush that gave rise to the subsequent Atana eruption (Lindsay, Schmitt, et al., 2001), but has undergone a separate, pre-eruptive evolution. The observation that both crystal-poor rhyolites (i.e., Toconao) and crystal-rich dacites (i.e., Atana and Tara) record similar patterns of diverse pre-existing mush amalgamation suggests that both eruption types are associated with destabilization of melt-rich magma lenses. Considering the spatial overlap of the studied eruption sources and the mid-crustal magmatic anomaly that presently underlies the Altiplano-Puna region (Figure 1), melt lenses may have been episodically reconstructed in the APMB, giving rise to invasive melts that disrupted more shallow level mush or sub-solidus intrusions.

Hydrous rhyolitic magma lenses have densities that are invariably lower than those of their host crystalline mushes, favoring the development of gravitational instabilities that may lead to magma transfer and eruption at the surface. Assessing the timescale over which melt lens instabilities develop in crystal mushes and comparing these estimates to our diffusion-derived maximum crystal residence times provides an opportunity to constrain the stability window for the presence of eruptible magma prior to large magnitude eruptions. Using analog experiments, Seropian et al. (2018) derived a formalism to calculate the timescales for the development of Rayleigh Taylor instabilities (RTI) in a case where the wavelength of the instability is larger than the width of the intrusion (confined case). The characteristic RTI time, over which the amplitude increases by a factor of  $e$  ( $\sim 2.72$ ), is given by

$$t_{\text{RTI,conf}} = \frac{6 \pi \mu}{\Delta \rho g L},$$

where  $\mu$  is the viscosity of crystal mush in Pa s,  $\Delta \rho$  is the difference of crystal mush and melt lens density ( $\text{kg m}^{-3}$ ),  $g$  is the acceleration of gravity in  $\text{m s}^{-2}$ , and  $L$  is the diameter of the melt layer in m. Timescales for cases in which the instability wavelength is smaller than the width of the melt length (unconfined case) can be calculated based on earlier work (Whitehead & Luther, 1975) by:

$$t_{\text{RTI,unconf.}} = \frac{\mu}{0.232 g \Delta \rho h} \varepsilon^{-\frac{1}{3}},$$

where  $h$  is the thickness of the melt lens in meters and  $\varepsilon$  is the ratio of mush and melt lens viscosities in Pa s. In a first step, to constrain the impact of modeling variables, we explored a range of relevant variables for rhyolitic melt lenses using a Monte Carlo approach, calculating 10,000 random combinations of mush viscosities ( $10^{14}$ – $10^{19}$  Pa s), mush and melt densities ( $2,600$ – $3,000 \text{ kg m}^{-3}$ ;  $2,000$ – $2,500 \text{ kg m}^{-3}$ ), and melt lens diameters ( $5$ – $80 \text{ km}$ ) for the confined case (Figure 12a), and melt lens thickness between  $50$  and  $500 \text{ m}$  in the unconfined case (Figure 12b). Confined instability timescales vary over a vast range of timescales spanning years (at the lowest mush viscosities) to several hundred thousand years, while calculated instability timescales for the unconfined case are as short as  $7 \text{ hr}$  up to  $62 \text{ days}$  for the parameter space under consideration.

To better constrain instability timescales relevant in the more specific cases of the Atana and Tara eruptions, we calculated the melt density for these events using average groundmass glass analyses (Grocke, de, Silva, Wallace, et al., 2017; Lindsay, Schmitt, et al., 2001) and partial molar volumes of the chemical components. The density calculations were performed using  $3 \text{ kbar}$  pressure,  $4$ – $5 \text{ wt.}\%$   $\text{H}_2\text{O}$ , and temperatures of  $754^\circ\text{C}$  and  $852^\circ\text{C}$  for Atana and Tara, respectively. Geophysical estimates of mush viscosities for the APMB have been constrained to be on the order of  $10^{16}$ – $10^{17} \text{ Pa s}$  (Gottsmann et al., 2017). Although the diameter and thickness of the melt layer that accumulated in the mush prior to the eruptions are unknown, the diameter of the source calderas and eruptive volumes may be used as proxies. If the collapse caldera diameter  $60 \times 35 \text{ km}$  for Atana and  $20 \times 30 \text{ km}$  for Tara reflects the size of the accumulating melt lens, and considering the DRE erupted melt volume for both eruptions,

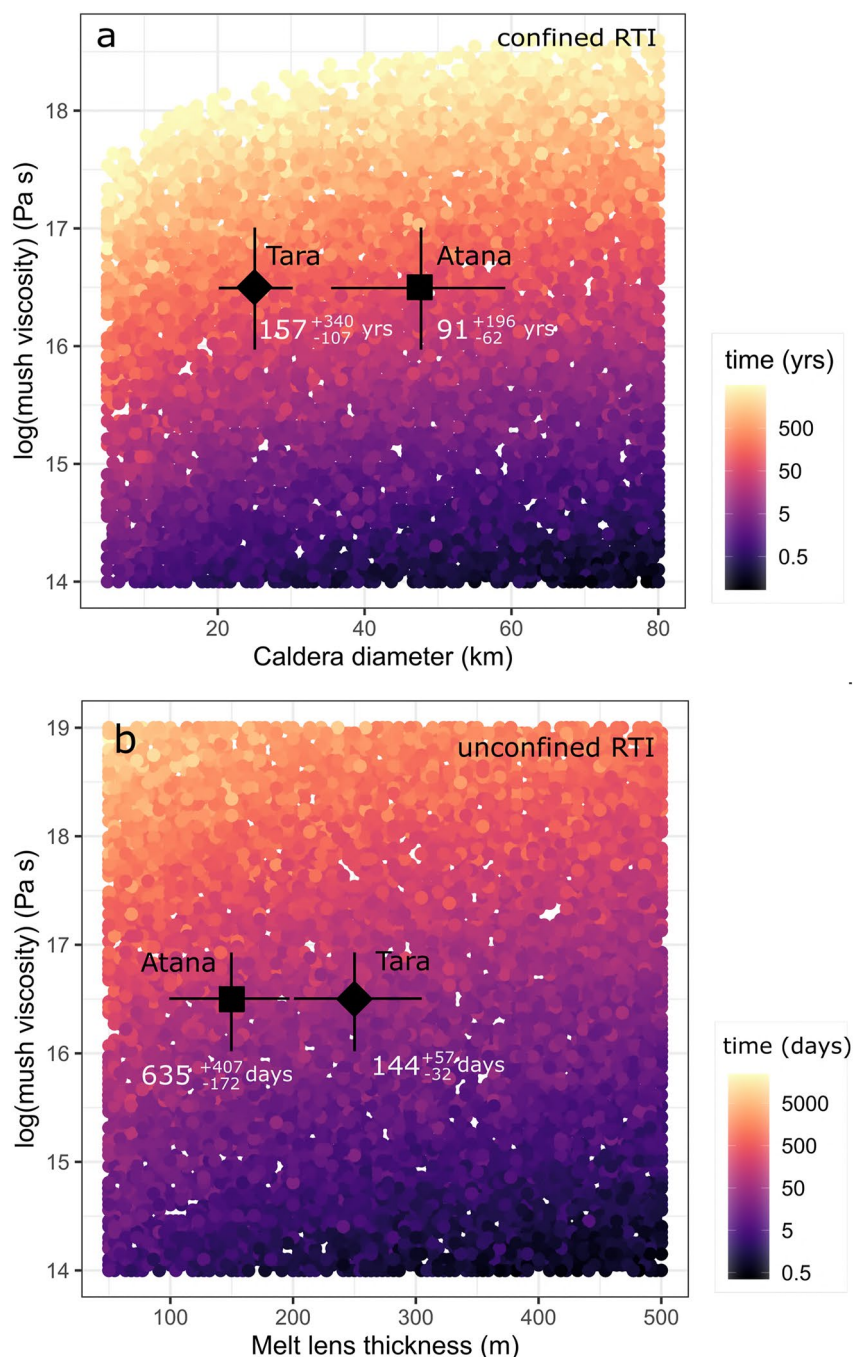


**Figure 12.** Gravitational instability timescales of melt lenses in crystal mush. Results are shown for the Atana (black square) and Tara (black diamond) eruptions superimposed on Monte Carlo simulations color-coded for time. Parameters used in the modeling are discussed in the main text. (a) Log mush viscosity versus caldera diameter (i.e., approximately diameter of the melt lens) for confined Rayleigh Taylor Instabilities where the wavelength is larger than the diameter of the melt lens (Seropian et al., 2018). For the sake of clarity only timescales <1000 years are shown. (b) Log mush viscosity versus melt lens thickness (calculated from erupted volume and caldera diameter for Atana and Tara). Timescales (days) are for an unconfined case, where the wavelength of the gravitational instability is smaller than the length of the melt lens.

cylindrical (volume =  $\pi r^2 h$ , where  $r$  and  $h$  are the radius and height) and ellipsoidal melt lenses (Volume =  $4/3 \pi a b c$ , where  $a$ ,  $b$ ,  $c$  are the semi-axes) would require a thickness of 130–170 m for Atana and 220–300 m for Tara. Caldera dimensions for the Toconao eruption are unknown due to superposition with the younger and much larger La Pacana caldera. However, based on an erupted DRE volume of 1,600 km<sup>3</sup>, the collapse structure can be

expected to be smaller than the Guacha II caldera, which would result in longer instability timescales (Figure 12). Our calculations indicate that instability timescales in the confined case are on the order of 50–500 years for Tara and 30–300 years for Atana. Unconfined instability timescales for both eruptions are significantly shorter on the order of days to a few years. Both cases are consistent with a time window for the presence of eruptible magma in crystal mushes that is much shorter than the maximum crystal residence time (decades to centuries) based on Sr isotope diffusion, in keeping with the emerging view that eruptible magmas are ephemeral in nature and develop over timescales relevant for volcano monitoring (van Zalinge et al., 2022).

#### 5.4. Detectability of Precursors to Supereruptions

Given the lack of observational experience with past large-volume eruptions, it remains unclear if we are currently capable of detecting the evolution toward a pending supereruption by geophysical volcano monitoring techniques. Although large-scale geophysical unrest has been observed prior to comparatively small explosive eruptions like Pinatubo in 1991 (McNutt, 1996), suggesting that similar features may be extrapolated to larger eruptions, the magnitude, timeframe and type of signals that may be observed remains obscure. Our petrological finding of a common pattern in melt-mush amalgamation in the runup to three large magnitude eruptions can be tested against the resolution of different geophysical monitoring techniques. Tomographic imaging by seismic and magnetotelluric methods has revealed that many large caldera complexes are underlain by massive mush accumulations, but are mostly comprised of mush at low melt fraction within the resolution of these methods (e.g., Toba: Jaxybulatov et al., 2014; Koulakov et al., 2016; Yellowstone: Farrell et al., 2014; Huang et al., 2015; APVC: Pritchard et al., 2018). As discussed above, considering the dimensions of the source calderas for the Atana and Tara eruptions, melt and eruptible magma lenses of not more than a few hundred meters thickness can be expected, which even under favorable seismic or magnetotelluric network configurations will be beyond the resolution of these methods (Lowenstern et al., 2017). Alternatively, the assembly of melt lenses and/or amalgamation of eruptible magma may create ground deformation pattern, which are now routinely measured in volcanic settings by GPS or satellite-based interferometry (Poland & Zebker, 2022). The detectability of such a signal in association with the accumulation of melt lenses and disruption of pre-existing mush pockets depends on various factors, including the magnitude of thermally controlled viscoelastic effects, which should be prevalent in crystal mushes, and potential exchange flow of upwards percolating melt and downwards displacement of crystalline materials. While much work has been focused on quantifying thermo-mechanical controls on surface

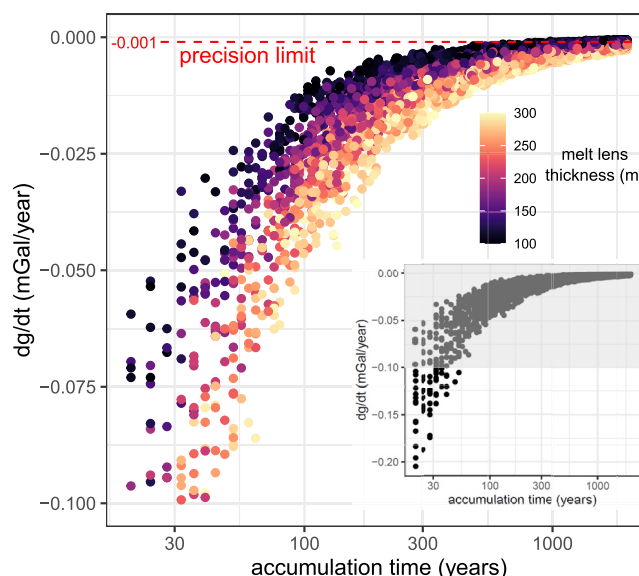


**Figure 13.** Gravity effect of an accumulating melt lens in crystal mush. Monte Carlo results are shown for the rate of change in gravitational acceleration ( $dg/dt$ ) in mGal/year vs. the accumulation time of melt lenses. Color coding reflects the thickness of the accumulated lens. The limit of precision for state-of-the-art gravimeters of  $-0.001$  mGal is indicated as a red dashed line. The inset shows the full range of  $dg/dt$  calculated over the parameter space considered. Only the gray shaded area is shown to aid comparison with the precision of gravimeters.



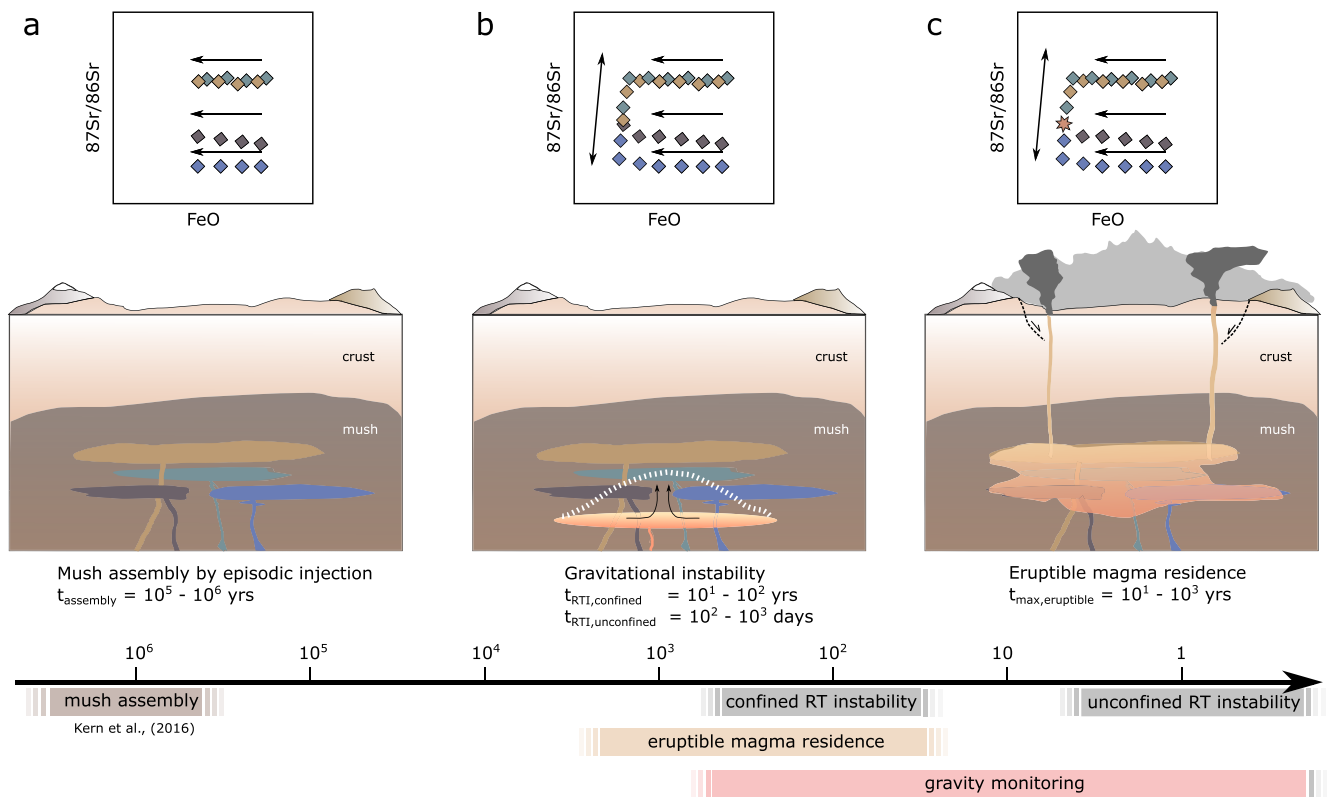


**Figure 14.** Conceptual summary of processes and timescales beneath the APVC. (a) Long-term mush accumulation on timescales of  $10^5$ – $10^6$  years as indicated by zircon geochronology (Kern et al., 2016). Pulsed injection of magma batches leads to spatial and temporal heterogeneity i.e., reflected in different isotopic compositions of crystal cores due to differing degrees of assimilation of local pre-magmatic crust. (b) Accumulating melt lenses develop gravitational instabilities over timescales of 10– $10^2$  years (confined case) or up to  $10^2$ – $10^3$  days (unconfined case). Amalgamation of previously intruded heterogeneous mush pockets leads to the formation of common rims in crystals. The scale of mush-crystal uptake can be limited (crystal-poor Toconao rhyolite) or severe (crystal-rich Atana and Tara dacite). (c) Eruptible magma emerges by hybridization of rhyolite melt and pre-existing mush pockets. Residence time of eruptible magma in the crust is on the order of 10– $10^3$  years.

deformation patterns (Del Negro et al., 2009; Head et al., 2019; Hickey et al., 2016; Morales Rivera et al., 2019), and integration of petrological models with surface geodetic studies (Townsend, 2022; Trasatti et al., 2019; Weber & Castro, 2017), deformation sources are typically modeled as an overpressure boundary condition on a cavity representing a magma body. New coupled models of melt flow in crystal mushes and ground deformation are required to test if destabilization of melt lenses could create large scale uplift and subsidence patterns such as those observed in the APVC.

The accumulation of a melt lens followed by invasive disruption of crystal mush could lead to a measurable change in the gravitational field, given that mushes and rhyolite melts have different densities. To quantify the magnitude of such an effect, we modeled the change in the gravitational acceleration ( $g$ ), caused by a cylindrical, low-density melt layer in higher density crystal mush (Telford et al., 1990):

$$g = 2 \pi G \Delta \rho \left\{ L + (z^2 + R^2)^{\frac{1}{2}} - [(z + L)^2 + R^2]^{\frac{1}{2}} \right\},$$

where  $G$  is the gravitational constant ( $6.67 \times 10^{-11} \text{ m}^3 \text{ kg}^{-1} \text{ s}^{-2}$ ),  $\Delta \rho$  is the density contrast of melt and mush ( $-300$  to  $-500 \text{ kg m}^{-3}$ ),  $L$  is the thickness of the melt layer (100–300 m),  $R$  is the diameter (20–50 km), and  $z$  is the depth of the cylinder top below the surface (10 km if not stated otherwise). Depth estimates for the Atana and Tara magmas are prone to high uncertainties, but are of secondary importance in the gravity calculations (Figure S4 in Supporting Information S1). We used 10,000 random combinations of the parameters given above to quantify the gravity effect of melt lens accumulation over a timeframe of 20–2000 years (Figure 13). Depending on the thickness of the lens, accumulation in less than 100 years results in strong gravity effects on the order of  $-0.20$  to  $-0.02 \text{ mGal/year}$ . Long-term growth over centennial and millennial timescales results in lower gravity

effects, but ~90% of the calculations yield gravity signals that are within the current precision limit of modern gravimeters (up to  $-0.001$  mGal; Greco et al., 2020). Our calculations indicate that even in the case of melt lens accumulation over several centuries, yearly changes in the gravitational acceleration (mGal/year) are potentially large enough to be detected. Thus, from a practical point of view, repeated gravity monitoring of caldera volcanoes over several years may resolve the process of melt lens accumulation and destabilization in crystal mushes. We suggest that high-precision gravity monitoring may provide crucial insights to evaluate if one or more of Earth's large caldera complexes are currently in the process of accumulating eruptible magma. In summary, although large magmatic mush systems are built up over prolonged periods of time on the order of several million years (e.g., Kern et al., 2016), our geochemical reconstructions and modeling indicate that the cycles of eruptible magma residence and melt lens accumulation destabilization are comparable and potentially detectable using gravity measurements (Figure 14).

## 6. Conclusions

A conceptual summary of this study is provided in Figure 14. Based on our petrological analysis and geophysical model calculations, we draw the following conclusions:

1. Sr-isotopes in plagioclase crystals from three Central Andean large magnitude eruptions (Atana, Tara, Toconao) reveal a recurrent pattern of large isotopic diversity in cores that converge in steep gradients toward common values in crystal rims. This suggests that previously intruded, isotopically distinct mush batches with spatially and/or temporally distinct histories have been homogenized and mobilized by an invasive rhyolite carrier melt before each eruption.
2. Isotopic compositions of glasses and plagioclase, as well as the plagioclase An-FeO systematics, show that the Toconao ignimbrite does not simply represent an extracted liquid from the mush that produced the subsequent Atana eruption. Instead, these two eruptions tapped distinct environments of the batholithic reservoir.
3. Most plagioclase crystals cannot have spent more time in the eruptible magma than decades to centuries for the Atana and Tara ignimbrites, and centuries to several millennia for the Toconao eruption. These maximum crystal residence timescales provide an upper limit for the observation window for eruptible magma in these systems. Destabilization of rhyolite melt lenses in crystal mush can proceed on timescales of years to centuries, typically shorter than the diffusion estimates, suggesting that eruptible magma pockets are ephemeral.
4. Calculations based on caldera dimensions and DRE erupted volumes, indicate that in the case of the Atana and Tara eruptions, the size of melt lenses and eruptible magma pockets was likely below the resolution of seismic and geodetic imaging techniques currently employed. The gravity effect of eruptible magma accumulation may, however, be resolved using state-of-the-art instrumentation under favorable conditions.

## Acknowledgments

G.W. would like to thank the Swiss National Science Foundation for funding through an Early Postdoc. Mobility Fellowship (project number: P2GEP2\_195238). J.B. acknowledges funding from a Royal Society Research Professorship (RP/R1201048). D.B. was funded through a NERC CASE studentship and the European Research Council (ISONEB ERC Adv 321209 and PROCOMM ERC PoC 862389). The authors would like to thank Steve Sparks, Jo Gottsmann, Matt Jackson, David Pyle, Mike Cassidy, and Tamsin Mather for valuable discussion and suggestions regarding various aspects of this work. Tim Elliott is thanked for support of this project and comments that helped to improve the quality of the manuscript. Victoria Smith is acknowledged for support during EPMA analysis at Oxford. We thank Marie Edmonds for rapid editorial handling, Georg Zellmer and two anonymous referees for constructive comments that helped to improve this work.

## Conflict of Interest

The authors declare no conflicts of interest relevant to this study.

## Data Availability Statement

All data used in this study are available in the electronic supplementary materials to this article and in the *EarthChem* data repository (EPMA data: <https://doi.org/10.26022/IEDA/112752>, Sr-isotope data: <https://doi.org/10.26022/IEDA/112753>).

## References

- Allan, A. S. R., Barker, S. J., Millet, M.-A., Morgan, D. J., Rooyackers, S. M., Schipper, C. I., & Wilson, C. J. N. (2017). A cascade of magmatic events during the assembly and eruption of a super-sized magma body. *Contributions to Mineralogy and Petrology*, 172(7), 49. <https://doi.org/10.1007/s00410-017-1367-8>
- Allan, A. S. R., Morgan, D. J., Wilson, C. J. N., & Millet, M.-A. (2013). From mush to eruption in centuries: Assembly of the super-sized Oruanui magma body. *Contributions to Mineralogy and Petrology*, 166(1), 143–164. <https://doi.org/10.1007/s00410-013-0869-2>
- Andersen, D. J., Lindsley, D. H., & Davidson, P. M. (1993). QUILF: A pascal program to assess equilibria among Fe□Mg□Mn□Ti oxides, pyroxenes, olivine, and quartz. *Computers and Geosciences*, 19(9), 1333–1350. [https://doi.org/10.1016/0098-3004\(93\)90033-2](https://doi.org/10.1016/0098-3004(93)90033-2)

- Annen, C. (2009). From plutons to magma chambers: Thermal constraints on the accumulation of eruptible silicic magma in the upper crust. *Earth and Planetary Science Letters*, 284(3–4), 409–416. <https://doi.org/10.1016/j.epsl.2009.05.006>
- Annen, C., Blundy, J. D., & Sparks, R. S. J. (2006). The genesis of intermediate and silicic magmas in deep crustal hot zones. *Journal of Petrology*, 47(3), 505–539. <https://doi.org/10.1093/petrology/egi084>
- Bachmann, O., & Bergantz, G. W. (2004). On the origin of crystal-poor rhyolites: Extracted from batholithic crystal mushes. *Journal of Petrology*, 45(8), 1565–1582. <https://doi.org/10.1093/petrology/egh019>
- Bachmann, O., & Bergantz, G. W. (2006). Gas percolation in upper-crustal silicic crystal mushes as a mechanism for upward heat advection and rejuvenation of near-solidus magma bodies. *Journal of Volcanology and Geothermal Research*, 149(1), 85–102. <https://doi.org/10.1016/j.jvolgeores.2005.06.002>
- Bachmann, O., & Bergantz, G. W. (2008). Rhyolites and their source mushes across tectonic settings. *Journal of Petrology*, 49(12), 2277–2285. <https://doi.org/10.1093/petrology/egn068>
- Bachmann, O., Dungan, M. A., & Lipman, P. W. (2002). The Fish Canyon magma body, San Juan volcanic field, Colorado: Rejuvenation and eruption of an upper-crustal batholith. *Journal of Petrology*, 43(8), 1469–1503. <https://doi.org/10.1093/petrology/43.8.1469>
- Bachmann, O., & Huber, C. (2019). The inner workings of crustal distillation columns; the physical mechanisms and rates controlling phase separation in silicic magma reservoirs. *Journal of Petrology*, 60(1), 3–18. <https://doi.org/10.1093/petrology/egy103>
- Barker, S. J., Wilson, C. J. N., Morgan, D. J., & Rowland, J. V. (2016). Rapid priming, accumulation, and recharge of magma driving recent eruptions at a hyperactive caldera volcano. *Geology*, 44(4), 323–326. <https://doi.org/10.1130/G37382.1>
- Bevan, D., Coath, C. D., Lewis, J., Schwieters, J., Lloyd, N., Craig, G., et al. (2021). In situ Rb–Sr dating by collision cell, multicollection inductively-coupled plasma mass-spectrometry with pre-cell mass-filter, (CC-MC-ICPMS/MS). *Journal of Analytical Atomic Spectrometry*, 36(5), 917–931. <https://doi.org/10.1039/D1JA00006C>
- Bindeman, I. N., Davis, A. M., & Drake, M. J. (1998). Ion microprobe study of plagioclase-basalt partition experiments at natural concentration levels of trace elements. *Geochimica et Cosmochimica Acta*, 62(7), 1175–1193. [https://doi.org/10.1016/S0016-7037\(98\)00047-7](https://doi.org/10.1016/S0016-7037(98)00047-7)
- Black, B. A., Lamarque, J.-F., Marsh, D. R., Schmidt, A., & Bardeen, C. G. (2021). Global climate disruption and regional climate shelters after the Toba supereruption. *Proceedings of the National Academy of Sciences*, 118(29), e2013046118. <https://doi.org/10.1073/pnas.2013046118>
- Brandmeier, M., & Wörner, G. (2016). Compositional variations of ignimbrite magmas in the Central Andes over the past 26 Ma—A multivariate statistical perspective. *Lithos*, 262, 713–728. <https://doi.org/10.1016/j.lithos.2016.07.011>
- Burgisser, A., & Bergantz, G. W. (2011). A rapid mechanism to remobilize and homogenize highly crystalline magma bodies. *Nature*, 471(7337), 212–215. <https://doi.org/10.1038/nature09799>
- Caricchi, L., Annen, C., Blundy, J., Simpson, G., & Pinel, V. (2014). Frequency and magnitude of volcanic eruptions controlled by magma injection and buoyancy. *Nature Geoscience*, 7(2), 126–130. <https://doi.org/10.1038/ngeo2041>
- Caricchi, L., & Blundy, J. (2015). Experimental petrology of monotonous intermediate magmas. *Geological Society, London, Special Publications*, 422(1), 105–130. <https://doi.org/10.1144/SP422.9>
- Cashman, K., & Blundy, J. (2013). Petrological cannibalism: The chemical and textural consequences of incremental magma body growth. *Contributions to Mineralogy and Petrology*, 166(3), 703–729. <https://doi.org/10.1007/s00410-013-0895-0>
- Cashman, K. V., Sparks, R. S. J., & Blundy, J. D. (2017). Vertically extensive and unstable magmatic systems: A unified view of igneous processes. *Science*, 355(6331), eaag3055. <https://doi.org/10.1126/science.aag3055>
- Chadwick, J. P., Troll, V. R., Ginibre, C., Morgan, D., Gertisser, R., Waight, T. E., & Davidson, J. P. (2007). Carbonate assimilation at Merapi Volcano, Java, Indonesia: Insights from crystal isotope stratigraphy. *Journal of Petrology*, 48(9), 1793–1812. <https://doi.org/10.1093/petrology/egm038>
- Chamberlain, K. J., Morgan, D. J., & Wilson, C. J. N. (2014). Timescales of mixing and mobilisation in the Bishop Tuff magma body: Perspectives from diffusion chronometry. *Contributions to Mineralogy and Petrology*, 168(1), 1034. <https://doi.org/10.1007/s00410-014-1034-2>
- Charlier, B. L. A., Bachmann, O., Davidson, J. P., Dungan, M. A., & Morgan, D. J. (2007). The upper crustal evolution of a large silicic magma body: Evidence from crystal-scale Rb–Sr isotopic heterogeneities in the Fish Canyon magmatic system, Colorado. *Journal of Petrology*, 48(10), 1875–1894. <https://doi.org/10.1093/petrology/egm043>
- Cherniak, D. J., & Watson, E. B. (1994). A study of strontium diffusion in plagioclase using Rutherford backscattering spectroscopy. *Geochimica et Cosmochimica Acta*, 58(23), 5179–5190. [https://doi.org/10.1016/0016-7037\(94\)90303-4](https://doi.org/10.1016/0016-7037(94)90303-4)
- Claiborne, L. L., Miller, C. F., & Wooden, J. L. (2010). Trace element composition of igneous zircon: A thermal and compositional record of the accumulation and evolution of a large silicic batholith, Spirit Mountain, Nevada. *Contributions to Mineralogy and Petrology*, 160(4), 511–531. <https://doi.org/10.1007/s00410-010-0491-5>
- Comeau, M. J., Unsworth, M. J., & Cordell, D. (2016). New constraints on the magma distribution and composition beneath Volcán Uturuncu and the southern Bolivian Altiplano from magnetotelluric data. *Geosphere*, 12(5), 1391–1421. <https://doi.org/10.1130/GES01277.1>
- Comeau, M. J., Unsworth, M. J., Ticona, F., & Sunagua, M. (2015). Magnetotelluric images of magma distribution beneath Volcán Uturuncu, Bolivia: Implications for magma dynamics. *Geology*, 43(3), 243–246. <https://doi.org/10.1130/G36258.1>
- Cooper, G. F., Morgan, D. J., & Wilson, C. J. N. (2017). Rapid assembly and rejuvenation of a large silicic magmatic system: Insights from mineral diffusive profiles in the Kidnappers and Rocky Hill deposits, New Zealand. *Earth and Planetary Science Letters*, 473, 1–13. <https://doi.org/10.1016/j.epsl.2017.05.036>
- Costa, F., Dohmen, R., & Chakraborty, S. (2008). Time scales of magmatic processes from modeling the zoning patterns of crystals. *Reviews in Mineralogy and Geochemistry*, 69(1), 545–594. <https://doi.org/10.2138/rmg.2008.69.14>
- Davidson, J., Tepley, F., Palacz, Z., & Meffan-Main, S. (2001). Magma recharge, contamination and residence times revealed by in situ laser ablation isotopic analysis of feldspar in volcanic rocks. *Earth and Planetary Science Letters*, 184(2), 427–442. [https://doi.org/10.1016/S0012-821X\(00\)00333-2](https://doi.org/10.1016/S0012-821X(00)00333-2)
- Davidson, J. P., Morgan, D. J., Charlier, B. L. A., Harlou, R., & Hora, J. M. (2007). Microsampling and isotopic analysis of igneous rocks: Implications for the study of magmatic systems. *Annual Review of Earth and Planetary Sciences*, 35(1), 273–311. <https://doi.org/10.1146/annurev.earth.35.031306.140211>
- Del Negro, C., Currenti, G., & Scandura, D. (2009). Temperature-dependent viscoelastic modeling of ground deformation: Application to Etna volcano during the 1993–1997 inflation period. *Physics of the Earth and Planetary Interiors*, 172(3), 299–309. <https://doi.org/10.1016/j.pepi.2008.10.019>
- del Potro, R., Diez, M., Blundy, J., Camacho, A. G., & Gottsmann, J. (2013). Diapiric ascent of silicic magma beneath the Bolivian Altiplano. *Geophysical Research Letters*, 40(10), 2044–2048. <https://doi.org/10.1002/grl.50493>
- de Silva, S. L. (1989). Geochronology and stratigraphy of the ignimbrites from the 21°30'S to 23°30'S portion of the Central Andes of northern Chile. *Journal of Volcanology and Geothermal Research*, 37(2), 93–131. [https://doi.org/10.1016/0377-0273\(89\)90065-6](https://doi.org/10.1016/0377-0273(89)90065-6)

- de Silva, S. L., & Gosnold, W. D. (2007). Episodic construction of batholiths: Insights from the spatiotemporal development of an ignimbrite flare-up. *Journal of Volcanology and Geothermal Research*, 167(1–4), 320–335. <https://doi.org/10.1016/j.jvolgeores.2007.07.015>
- de Silva, S. L., & Kay, S. M. (2018). Turning up the heat: High-flux magmatism in the Central Andes. *Elements*, 14(4), 245–250. <https://doi.org/10.2138/gselements.14.4.245>
- De Silva, S., Zandt, G., Trumbull, R., Viramonte, J. G., Salas, G., & Jiménez, N. (2006). Large ignimbrite eruptions and volcano-tectonic depressions in the Central Andes: A thermomechanical perspective. *Geological Society, London, Special Publications*, 269(1), 47–63. <https://doi.org/10.1144/GSL.SP.2006.269.01.04>
- Dohmen, R., & Blundy, J. (2014). A predictive thermodynamic model for element partitioning between plagioclase and melt as a function of pressure, temperature and composition. *American Journal of Science*, 314(9), 1319–1372. <https://doi.org/10.2475/09.2014.04>
- Dohmen, R., Faak, K., & Blundy, J. D. (2017). Chronometry and speedometry of magmatic processes using chemical diffusion in olivine, plagioclase and pyroxenes. *Reviews in Mineralogy and Geochemistry*, 83(1), 535–575. <https://doi.org/10.2138/rmg.2017.83.16>
- Druitt, T. H., Costa, F., Deloule, E., Dungan, M., & Scaillet, B. (2012). Decadal to monthly timescales of magma transfer and reservoir growth at a caldera volcano. *Nature*, 482(7383), 77–80. <https://doi.org/10.1038/nature10706>
- Dufek, J., & Bachmann, O. (2010). Quantum magmatism: Magmatic compositional gaps generated by melt-crystal dynamics. *Geology*, 38(8), 687–690. <https://doi.org/10.1130/G30831.1>
- Edmonds, M., Cashman, K. V., Holness, M., & Jackson, M. (2019). Architecture and dynamics of magma reservoirs. *Philosophical Transactions of the Royal Society A: Mathematical, Physical & Engineering Sciences*, 377(2139), 20180298. <https://doi.org/10.1098/rsta.2018.0298>
- Elburg, M., Vroon, P., van der Wagt, B., & Tchalikian, A. (2005). Sr and Pb isotopic composition of five USGS glasses (BHVO-2G, BIR-1G, BCR-2G, TB-1G, NKT-1G). *Chemical Geology*, 223(4), 196–207. <https://doi.org/10.1016/j.chemgeo.2005.07.001>
- Farrell, J., Smith, R. B., Husen, S., & Diehl, T. (2014). Tomography from 26 years of seismicity revealing that the spatial extent of the Yellowstone crustal magma reservoir extends well beyond the Yellowstone caldera. *Geophysical Research Letters*, 41(9), 3068–3073. <https://doi.org/10.1002/2014GL059588>
- Freymuth, H., Brandmeier, M., & Wörner, G. (2015). The origin and crust/mantle mass balance of Central Andean ignimbrite magmatism constrained by oxygen and strontium isotopes and erupted volumes. *Contributions to Mineralogy and Petrology*, 169(6), 58. <https://doi.org/10.1007/s00410-015-1152-5>
- Gardeweg, M., & Ramírez, C. F. (1987). La Pacana caldera and the Atana ignimbrite? A major ash-flow and resurgent caldera complex in the Andes of northern Chile. *Bulletin of Volcanology*, 49(3), 547–566. <https://doi.org/10.1007/BF01080449>
- Ghiorsio, M. S. (1984). Activity/composition relations in the ternary feldspars. *Contributions to Mineralogy and Petrology*, 87(3), 282–296. <https://doi.org/10.1007/BF00373061>
- Ghiorsio, M. S., & Evans, B. W. (2008). Thermodynamics of rhombohedral oxide solid solutions and a revision of the FE-TI two-oxide geothermometer and oxygen-barometer. *American Journal of Science*, 308(9), 957–1039. <https://doi.org/10.2475/09.2008.01>
- Giletti, B. J., & Casserly, J. E. D. (1994). Strontium diffusion kinetics in plagioclase feldspars. *Geochimica et Cosmochimica Acta*, 58(18), 3785–3793. [https://doi.org/10.1016/0016-7037\(94\)90363-8](https://doi.org/10.1016/0016-7037(94)90363-8)
- Gottsmann, J., Blundy, J., Henderson, S., Pritchard, M. E., & Sparks, R. S. J. (2017). Thermomechanical modeling of the Altiplano-Puna deformation anomaly: Multiparameter insights into magma mush reorganization. *Geosphere*, 13(4), 1042–1065. <https://doi.org/10.1130/GE.S01420.1>
- Greco, F., Carbone, D., Cannavò, F., Messina, A. A., & Siligato, G. (2020). *Absolute and relative gravity measurements at volcanoes: Current state and new developments under the NEWTON-g project* (pp. 1–7). Springer. [https://doi.org/10.1007/1345\\_2020\\_126](https://doi.org/10.1007/1345_2020_126)
- Groccke, S. B., de Silva, S. L., Iriarte, R., Lindsay, J. M., & Cottrell, E. (2017). Catastrophic caldera-forming (CCF) monotonous silicic magma reservoirs: Geochemical and petrological constraints on heterogeneity, magma dynamics, and eruption dynamics of the 3–49 Ma Tara supereruption, Guacha II caldera, SW Bolivia. *Journal of Petrology*, 58(2), 227–260. <https://doi.org/10.1093/petrology/egx012>
- Groccke, S. B., de Silva, S. L., Wallace, P. J., Cottrell, E., & Schmitt, A. K. (2017). Catastrophic caldera-forming (CCF) monotonous silicic magma reservoirs: Constraints from volatiles in melt inclusions from the 3–49 Ma Tara supereruption, Guacha II caldera, SW Bolivia. *Journal of Petrology*, 58(11), 2115–2142. <https://doi.org/10.1093/petrology/egy003>
- Gualda, G. A. R., & Sutton, S. R. (2016). The year leading to a supereruption. *PLoS One*, 11(7), e0159200. <https://doi.org/10.1371/journal.pone.0159200>
- Hartung, E., Weber, G., & Caricchi, L. (2019). The role of H<sub>2</sub>O on the extraction of melt from crystallising magmas. *Earth and Planetary Science Letters*, 508, 85–96. <https://doi.org/10.1016/j.epsl.2018.12.010>
- Head, M., Hickey, J., Gottsmann, J., & Fournier, N. (2019). The influence of viscoelastic crustal rheologies on volcanic ground deformation: Insights from models of pressure and volume change. *Journal of Geophysical Research: Solid Earth*, 124(8), 8127–8146. <https://doi.org/10.1029/2019JB017832>
- Hickey, J., Gottsmann, J., & del Potro, R. (2013). The large-scale surface uplift in the Altiplano-Puna region of Bolivia: A parametric study of source characteristics and crustal rheology using finite element analysis. *Geochemistry, Geophysics, Geosystems*, 14(3), 540–555. <https://doi.org/10.1002/ggge.20057>
- Hickey, J., Gottsmann, J., Nakamichi, H., & Iguchi, M. (2016). Thermomechanical controls on magma supply and volcanic deformation: Application to Aira caldera, Japan. *Scientific Reports*, 6(1), 32691. <https://doi.org/10.1038/srep32691>
- Holland, T., & Blundy, J. (1994). Non-ideal interactions in calcic amphiboles and their bearing on amphibole-plagioclase thermometry. *Contributions to Mineralogy and Petrology*, 116(4), 433–447. <https://doi.org/10.1007/BF00310910>
- Huang, H.-H., Lin, F.-C., Schmandt, B., Farrell, J., Smith, R. B., & Tsai, V. C. (2015). The Yellowstone magmatic system from the mantle plume to the upper crust. *Science*, 348(6236), 773–776. <https://doi.org/10.1126/science.aaa5648>
- Huber, C., Bachmann, O., & Dufek, J. (2011). Thermo-mechanical reactivation of locked crystal mushes: Melting-induced internal fracturing and assimilation processes in magmas. *Earth and Planetary Science Letters*, 304(3–4), 443–454. <https://doi.org/10.1016/j.epsl.2011.02.022>
- Humphreys, M. C. S., Blundy, J. D., & Sparks, R. S. J. (2006). Magma evolution and open-system processes at Shiveluch Volcano: Insights from Phenocryst zoning. *Journal of Petrology*, 47(12), 2303–2334. <https://doi.org/10.1093/petrology/egl045>
- Jackson, M. D., Blundy, J., & Sparks, R. S. J. (2018). Chemical differentiation, cold storage and remobilization of magma in the Earth's crust. *Nature*, 564(7736), 405–409. <https://doi.org/10.1038/s41586-018-0746-2>
- Jaxybulatov, K., Shapiro, N. M., Koulakov, I., Mordret, A., Landès, M., & Sens-Schönfelder, C. (2014). A large magmatic sill complex beneath the Toba caldera. *Science*, 346(6209), 617–619. <https://doi.org/10.1126/science.1258582>
- Kay, S. M., Coira, B. L., Caffee, P. J., & Chen, C.-H. (2010). Regional chemical diversity, crustal and mantle sources and evolution of central Andean Puna plateau ignimbrites. *Journal of Volcanology and Geothermal Research*, 198(1–2), 81–111. <https://doi.org/10.1016/j.jvolgeores.2010.08.013>



- Kern, J. M., de Silva, S. L., Schmitt, A. K., Kaiser, J. F., Iriarte, A. R., & Economos, R. (2016). Geochronological imaging of an episodically constructed subvolcanic batholith: U-Pb in zircon chronochemistry of the Altiplano-Puna volcanic complex of the central Andes. *Geosphere*, 12(4), 1054–1077. <https://doi.org/10.1130/GES01258.1>
- Klemetti, E. W., & Clyne, M. A. (2014). Localized rejuvenation of a crystal mush recorded in zircon temporal and compositional variation at the Lassen Volcanic Center, Northern California. *PLoS One*, 9(12), e113157. <https://doi.org/10.1371/journal.pone.0113157>
- Koulakov, I., Kasatkina, E., Shapiro, N. M., Jaupart, C., Vasilevsky, A., El Khrepy, S., et al. (2016). The feeder system of the Toba supervolcano from the slab to the shallow reservoir. *Nature Communications*, 7(1), 12228. <https://doi.org/10.1038/ncomms12228>
- Lee, C.-T. A., Morton, D. M., Farner, M. J., & Moitra, P. (2015). Field and model constraints on silicic melt segregation by compaction/hindered settling: The role of water and its effect on latent heat release. *American Mineralogist*, 100(8–9), 1762–1777. <https://doi.org/10.2138/am-2015-5121>
- Lindsay, J. M., de Silva, S., Trumbull, R., Emmermann, R., & Wemmer, K. (2001). La Pacana caldera, N. Chile: A re-evaluation of the stratigraphy and volcanology of one of the world's largest resurgent calderas. *Journal of Volcanology and Geothermal Research*, 106(1–2), 145–173. [https://doi.org/10.1016/S0377-0273\(00\)00270-5](https://doi.org/10.1016/S0377-0273(00)00270-5)
- Lindsay, J. M., Schmitt, A. K., Trumbull, R. B., De Silva, S. L., Siebel, W., & Emmermann, R. (2001). Magmatic evolution of the La Pacana caldera system, Central Andes, Chile: Compositional variation of two cogenetic, large-volume felsic ignimbrites. *Journal of Petrology*, 42(3), 459–486. <https://doi.org/10.1093/petrology/42.3.459>
- Liu, M., & Yund, R. A. (1992). NaSi-CaAl interdiffusion in plagioclase. *American Mineralogist*, 77(3–4), 275–283.
- Liu, P.-P., Caricchi, L., Chung, S.-L., Li, X.-H., Li, Q.-L., Zhou, M.-F., et al. (2021). Growth and thermal maturation of the Toba magma reservoir. *Proceedings of the National Academy of Sciences*, 118(45), e2101695118. <https://doi.org/10.1073/pnas.2101695118>
- Lowenstern, J., Sisson, T., & Hurwitz, S. (2017). Probing magma reservoirs to improve volcano forecasts. *Eos Transactions American Geophysical Union*, 98. <https://doi.org/10.1029/2017EO085189>
- Lukács, R., Caricchi, L., Schmitt, A. K., Bachmann, O., Karakas, O., Guillong, M., et al. (2021). Zircon geochronology suggests a long-living and active magmatic system beneath the Ciomadul volcanic dome field (eastern-central Europe). *Earth and Planetary Science Letters*, 565, 116965. <https://doi.org/10.1016/j.epsl.2021.116965>
- Magee, C., Stevenson, C. T. E., Ebmeier, S. K., Keir, D., Hammond, J. O. S., Gottsmann, J. H., et al. (2018). Magma plumbing systems: A geophysical perspective. *Journal of Petrology*, 59(6), 1217–1251. <https://doi.org/10.1093/petrology/egy064>
- Marsh, B. D. (1981). On the crystallinity, probability of occurrence, and rheology of lava and magma. *Contributions to Mineralogy and Petrology*, 78(1), 85–98. <https://doi.org/10.1007/BF00371146>
- McKenzie, D. (1985). The extraction of magma from the crust and mantle. *Earth and Planetary Science Letters*, 74(1), 81–91. [https://doi.org/10.1016/0012-821x\(85\)90168-2](https://doi.org/10.1016/0012-821x(85)90168-2)
- McNutt, S. R. (1996). Seismic monitoring and eruption forecasting of volcanoes: A review of the state-of-the-art and case histories. In R. Scarpa & R. I. Tilling (Eds.), *Monitoring and mitigation of volcano hazards* (pp. 99–146). Springer. [https://doi.org/10.1007/978-3-642-80087-0\\_3](https://doi.org/10.1007/978-3-642-80087-0_3)
- Morales Rivera, A. M., Amelung, F., Albino, F., & Gregg, P. M. (2019). Impact of crustal rheology on temperature-dependent viscoelastic models of volcano deformation: Application to Taal Volcano, Philippines. *Journal of Geophysical Research: Solid Earth*, 124(1), 978–994. <https://doi.org/10.1029/2018JB016054>
- Papale, P. (2018). Global time-size distribution of volcanic eruptions on Earth. *Scientific Reports*, 8(1), 6838. <https://doi.org/10.1038/s41598-018-25286-y>
- Perez, W. A., & Dunn, T. (1996). Diffusivity of strontium, neodymium, and lead in natural rhyolite melt at 1.0 GPa. *Geochimica et Cosmochimica Acta*, 60(8), 1387–1397. [https://doi.org/10.1016/0016-7037\(96\)00016-6](https://doi.org/10.1016/0016-7037(96)00016-6)
- Perkins, J. P., Ward, K. M., de Silva, S. L., Zandt, G., Beck, S. L., & Finnegan, N. J. (2016). Surface uplift in the Central Andes driven by growth of the Altiplano Puna Magma Body. *Nature Communications*, 7(1), 13185. <https://doi.org/10.1038/ncomms13185>
- Pistone, M., Blundy, J., & Brooker, R. A. (2017). Water transfer during magma mixing events: Insights into crystal mush rejuvenation and melt extraction processes. *American Mineralogist*, 102(4), 766–776. <https://doi.org/10.2138/am-2017-5793>
- Poland, M. P., & Zebker, H. A. (2022). Volcano geodesy using InSAR in 2020: The past and next decades. *Bulletin of Volcanology*, 84(3), 27. <https://doi.org/10.1007/s00445-022-01531-1>
- Pritchard, M. E., de Silva, S. L., Michelfelder, G., Zandt, G., McNutt, S. R., Gottsmann, J., et al. (2018). Synthesis: PLUTONS: Investigating the relationship between pluton growth and volcanism in the Central Andes. *Geosphere*, 14(3), 954–982. <https://doi.org/10.1130/GES01578.1>
- Putirka, K. D. (2005). Igneous thermometers and barometers based on plagioclase + liquid equilibria: Tests of some existing models and new calibrations. *American Mineralogist*, 90(2–3), 336–346. <https://doi.org/10.2138/am.2005.1449>
- Ramos, F. C., Wolff, J. A., & Tollstrup, D. L. (2005). Sr isotope disequilibrium in Columbia River flood basalts: Evidence for rapid shallow-level open-system processes. *Geology*, 33(6), 457–460. <https://doi.org/10.1130/G21512.1>
- Rampino, M. R. (2002). Supereruptions as a threat to civilizations on Earth-like planets. *Icarus*, 156(2), 562–569. <https://doi.org/10.1006/icar.2001.6808>
- Rubin, A. E., Cooper, K. M., Till, C. B., Kent, A. J. R., Costa, F., Bose, M., et al. (2017). Rapid cooling and cold storage in a silicic magma reservoir recorded in individual crystals. *Science*, 356(6343), 1154–1156. <https://doi.org/10.1126/science.aam8720>
- Ruprecht, P., & Wörner, G. (2007). Variable regimes in magma systems documented in plagioclase zoning patterns: El Misti stratovolcano and Andahuasi monogenetic cones. *Journal of Volcanology and Geothermal Research*, 165(3–4), 142–162. <https://doi.org/10.1016/j.jvolgeores.2007.06.002>
- Russell, W. A., Papanastassiou, D. A., & Tombrello, T. A. (1978). Ca isotope fractionation on the Earth and other solar system materials. *Geochimica et Cosmochimica Acta*, 42(8), 1075–1090. [https://doi.org/10.1016/0016-7037\(78\)90105-9](https://doi.org/10.1016/0016-7037(78)90105-9)
- Salisbury, M. J., Jicha, B. R., de Silva, S. L., Singer, B. S., Jimenez, N. C., & Ort, M. H. (2011). <sup>40</sup>Ar/<sup>39</sup>Ar chronostratigraphy of Altiplano-Puna volcanic complex ignimbrites reveals the development of a major magmatic province. *Geological Society of America Bulletin*, 123(5–6), 821–840. <https://doi.org/10.1130/B30280.1>
- Schmitt, A., de Silva, S., Trumbull, R., & Emmermann, R. (2001). Magma evolution in the Purico ignimbrite complex, northern Chile: Evidence for zoning of a dacitic magma by injection of rhyolitic melts following mafic recharge. *Contributions to Mineralogy and Petrology*, 140(6), 680–700. <https://doi.org/10.1007/s004100000214>
- Self, S. (2006). The effects and consequences of very large explosive volcanic eruptions. *Philosophical Transactions of the Royal Society A: Mathematical, Physical & Engineering Sciences*, 364(1845), 2073–2097. <https://doi.org/10.1098/rsta.2006.1814>
- Self, S., & Blake, S. (2008). Consequences of explosive supereruptions. *Elements*, 4(1), 41–46. <https://doi.org/10.2113/GSELEMENTS.4.1.41>
- Seropian, G., Rust, A. C., & Sparks, R. S. J. (2018). The gravitational stability of lenses in magma mushes: Confined Rayleigh-Taylor instabilities. *Journal of Geophysical Research: Solid Earth*, 123(5), 3593–3607. <https://doi.org/10.1029/2018JB015523>

- Shamloo, H. I., & Till, C. B. (2019). Decadal transition from quiescence to supereruption: Petrologic investigation of the Lava Creek Tuff, Yellowstone Caldera, WY. *Contributions to Mineralogy and Petrology*, 174(4), 32. <https://doi.org/10.1007/s00410-019-1570-x>
- Sisson, T. W., & Bacon, C. R. (1999). Gas-driven filter pressing in magmas. *Geology*, 27(7), 613. [https://doi.org/10.1130/0091-7613\(1999\)027<0613:GDFPIM>2.3.CO;2](https://doi.org/10.1130/0091-7613(1999)027<0613:GDFPIM>2.3.CO;2)
- Sliwinski, J., Farsky, D., Lipman, P. W., Guillong, M., & Bachmann, O. (2019). Rapid magma generation or shared magmatic reservoir? Petrology and geochronology of the Rat Creek and Nelson Mountain Tuffs, CO, USA. *Frontiers in Earth Science*, 7, 271. <https://doi.org/10.3389/feart.2019.00271>
- Solano, J. M. S., Jackson, M. D., Sparks, R. S. J., & Blundy, J. (2014). Evolution of major and trace element composition during melt migration through crystalline mush: Implications for chemical differentiation in the crust. *American Journal of Science*, 314(5), 895–939. <https://doi.org/10.2475/05.2014.01>
- Solano, J. M. S., Jackson, M. D., Sparks, R. S. J., Blundy, J. D., & Annen, C. (2012). Melt segregation in deep crustal hot zones: A mechanism for chemical differentiation, crustal assimilation and the formation of evolved magmas. *Journal of Petrology*, 53(10), 1999–2026. <https://doi.org/10.1093/ptrology/egs041>
- Sparks, R. S. J., Annen, C., Blundy, J. D., Cashman, K. V., Rust, A. C., & Jackson, M. D. (2019). Formation and dynamics of magma reservoirs. *Philosophical Transactions of the Royal Society A: Mathematical, Physical & Engineering Sciences*, 377(2139), 20180019. <https://doi.org/10.1098/rsta.2018.0019>
- Sparks, R. S. J., Blundy, J. D., Cashman, K. V., Jackson, M., Rust, A., & Wilson, C. J. N. (2022). Large silicic magma bodies and very large magnitude explosive eruptions. *Bulletin of Volcanology*, 84(1), 8. <https://doi.org/10.1007/s00445-021-01510-y>
- Spera, F. J., & Bohron, W. A. (2018). Rejuvenation of crustal magma mush: A tale of multiply nested processes and timescales. *American Journal of Science*, 318(1), 90–140. <https://doi.org/10.2475/01.2018.05>
- Szymanowski, D., Ellis, B. S., Wotzlaw, J.-F., & Bachmann, O. (2019). Maturation and rejuvenation of a silicic magma reservoir: High-resolution chronology of the Kneeling Nun Tuff. *Earth and Planetary Science Letters*, 510, 103–115. <https://doi.org/10.1016/j.epsl.2019.01.007>
- Szymanowski, D., Wotzlaw, J.-F., Ellis, B. S., Bachmann, O., Guillong, M., & von Quadt, A. (2017). Protracted near-solidus storage and pre-eruptive rejuvenation of large magma reservoirs. *Nature Geoscience*, 10(10), 777–782. <https://doi.org/10.1038/ngeo3020>
- Taddeucci, J., Cimarelli, C., Alatorre-Ibargüengoitia, M. A., Delgado-Granados, H., Andronico, D., Del Bello, E., et al. (2021). Fracturing and healing of basaltic magmas during explosive volcanic eruptions. *Nature Geoscience*, 14(4), 248–254. <https://doi.org/10.1038/s41561-021-00708-1>
- Tapster, S., Condon, D. J., Naden, J., Noble, S. R., Petterson, M. G., Roberts, N. M. W., et al. (2016). Rapid thermal rejuvenation of high-crystallinity magma linked to porphyry copper deposit formation; evidence from the Koloula Porphyry Prospect, Solomon Islands. *Earth and Planetary Science Letters*, 442, 206–217. <https://doi.org/10.1016/j.epsl.2016.02.046>
- Telford, W. M., Telford, W. M., Geldart, L. P., & Sheriff, R. E. (1990). *Applied Geophysics*. Cambridge University Press.
- Tepley, F. J., III, Davidson, J. P., Tilling, R. I., & Arth, J. G. (2000). Magma mixing, recharge and eruption histories recorded in plagioclase phenocrysts from El Chichón Volcano, Mexico. *Journal of Petrology*, 41(9), 1397–1411. <https://doi.org/10.1093/ptrology/41.9.1397>
- Townsend, M. (2022). Linking surface deformation to thermal and mechanical magma chamber processes. *Earth and Planetary Science Letters*, 577, 117272. <https://doi.org/10.1016/j.epsl.2021.117272>
- Trasatti, E., Acocella, V., Di Vito, M. A., Del Gaudio, C., Weber, G., Aquino, I., et al. (2019). Magma degassing as a source of long-term seismicity at volcanoes: The Ischia Island (Italy) case. *Geophysical Research Letters*, 46(24), 14421–14429. <https://doi.org/10.1029/2019GL085371>
- van Zalinge, M. E., Cashman, K. V., & Sparks, R. S. J. (2018). Causes of fragmented crystals in ignimbrites: A case study of the Cardones ignimbrite, Northern Chile. *Bulletin of Volcanology*, 80(3), 22. <https://doi.org/10.1007/s00445-018-1196-2>
- van Zalinge, M. E., Mark, D. F., Sparks, R. S. J., Tremblay, M. M., Keller, C. B., Cooper, F. J., & Rust, A. (2022). Timescales for pluton growth, magma-chamber formation and super-eruptions. *Nature*, 608(7921), 87–92. <https://doi.org/10.1038/s41586-022-04921-9>
- Vigneresse, J. L., Barbey, P., & Cuney, M. (1996). Rheological transitions during partial melting and crystallization with application to felsic magma segregation and transfer. *Journal of Petrology*, 37(6), 1579–1600. <https://doi.org/10.1093/ptrology/37.6.1579>
- Villa, I. M., De Bièvre, P., Holden, N. E., & Renne, P. R. (2015). IUPAC-IUGS recommendation on the half life of <sup>87</sup>Rb. *Geochimica et Cosmochimica Acta*, 164, 382–385. <https://doi.org/10.1016/j.gca.2015.05.025>
- Waight, T. E., & Törnqvist, J. B. (2018). Sr isotope zoning in plagioclase from andesites at Cabo De Gata, Spain: Evidence for shallow and deep contamination. *Lithos*, 308–309, 159–167. <https://doi.org/10.1016/j.lithos.2018.03.007>
- Ward, K. M., Delph, J. R., Zandt, G., Beck, S. L., & Ducea, M. N. (2017). Magmatic evolution of a Cordilleran flare-up and its role in the creation of silicic crust. *Scientific Reports*, 7(1), 9047. <https://doi.org/10.1038/s41598-017-09015-5>
- Ward, K. M., Zandt, G., Beck, S. L., Christensen, D. H., & McFarlin, H. (2014). Seismic imaging of the magmatic underpinnings beneath the Altiplano-Puna volcanic complex from the joint inversion of surface wave dispersion and receiver functions. *Earth and Planetary Science Letters*, 404, 43–53. <https://doi.org/10.1016/j.epsl.2014.07.022>
- Waters, L. E., & Lange, R. A. (2015). An updated calibration of the plagioclase-liquid hygrometer-thermometer applicable to basalts through rhyolites. *American Mineralogist*, 100(10), 2172–2184. <https://doi.org/10.2138/am-2015-5232>
- Weber, G., Arce, J. L., Ulianov, A., & Caricchi, L. (2019). A recurrent magmatic pattern on observable timescales prior to Plinian eruptions from Nevado de Toluca (Mexico). *Journal of Geophysical Research: Solid Earth*, 124(11), 10999–11021. <https://doi.org/10.1029/2019JB017640>
- Weber, G., Caricchi, L., Arce, J. L., & Schmitt, A. K. (2020). Determining the current size and state of subvolcanic magma reservoirs. *Nature Communications*, 11(1), 5477. <https://doi.org/10.1038/s41467-020-19084-2>
- Weber, G., & Castro, J. M. (2017). Phase petrology reveals shallow magma storage prior to large explosive silicic eruptions at Hekla volcano, Iceland. *Earth and Planetary Science Letters*, 466, 168–180. <https://doi.org/10.1016/j.epsl.2017.03.015>
- Weber, G., Simpson, G., & Caricchi, L. (2020). Magma diversity reflects recharge regime and thermal structure of the crust. *Scientific Reports*, 10(1), 11867. <https://doi.org/10.1038/s41598-020-68610-1>
- Whitehead, J. A., Jr., & Luther, D. S. (1975). Dynamics of laboratory diapir and plume models. *Journal of Geophysical Research*, 80(5), 705–717. <https://doi.org/10.1029/jb080i005p00705>
- Wilke, M., & Behrens, H. (1999). The dependence of the partitioning of iron and europium between plagioclase and hydrous tonalitic melt on oxygen fugacity. *Contributions to Mineralogy and Petrology*, 137(1–2), 102–114. <https://doi.org/10.1007/s004100050585>
- Wilson, C. J. N., Cooper, G. F., Chamberlain, K. J., Barker, S. J., Myers, M. L., Illsley-Kemp, F., & Farrell, J. (2021). No single model for supersized eruptions and their magma bodies. *Nature Reviews Earth and Environment*, 2(9), 610–627. <https://doi.org/10.1038/s43017-021-00191-7>
- Wise, S. A., & Watters, R. L. (2012). *Certificate of analysis: Standard reference material 610*. National Institute of Standards and Technology.

- Wotzlaw, J.-F., Bindeman, I. N., Watts, K. E., Schmitt, A. K., Caricchi, L., & Schaltegger, U. (2014). Linking rapid magma reservoir assembly and eruption trigger mechanisms at evolved Yellowstone-type supervolcanoes. *Geology*, 42(9), 807–810. <https://doi.org/10.1130/G35979.1>
- Wotzlaw, J.-F., Schaltegger, U., Frick, D. A., Dungan, M. A., Gerdes, A., & Günther, D. (2013). Tracking the evolution of large-volume silicic magma reservoirs from assembly to supereruption. *Geology*, 41(8), 867–870. <https://doi.org/10.1130/G34366.1>
- Zandt, G., Leidig, M., Chmielowski, J., Baumont, D., & Yuan, X. (2003). Seismic detection and Characterization of the Altiplano-Puna magma body, central Andes. *Pure and Applied Geophysics*, 160(3), 789–807. <https://doi.org/10.1007/PL00012557>